TUNL REU X

RESEARCH REPORT

19 MAY 2024 – 27 JULY 2024

TRIANGLE UNIVERSITIES NUCLEAR LABORATORY

Duke University
North Carolina Central University
North Carolina State University
University of North Carolina at Chapel Hill

Box 90308, Durham, North Carolina 27708-0308, USA

The research described in this report is supported by the United States Department of Energy, Office of Science, under:

Grant No. DE-SC0010007 (Duke University High-Energy Physics Group),
Grant No. DE-FG02-97ER41033 (Duke University/TUNL),
Grant No. DE-FG02-97ER41042 (North Carolina State University), and
Grant No. DE-FG02-97ER41041 (University of North Carolina).

The TUNL Research Experiences for Undergraduates (REU) Program is supported by the National Science Foundation under:

Grant No. NSF-PHY-2150118.

Contents

Introduction

An important national goal is to develop a diverse, internationally competitive, and globally engaged workforce in science and engineering. The Research Experiences for Undergraduates (REU) program is part of the effort to achieve that goal. The REU program at the Triangle Universities Nuclear Laboratory (TUNL) and Duke University provides a ten-week opportunity for undergraduate students to pursue research in the areas of nuclear and particle physics. This allows promising physics majors to broaden their education through participation in research at the frontiers of these exciting scientific fields.

In 2024, thirteen students participated in the TUNL REU Program: nine spent the summer working on nuclear physics projects on the Duke campus, while the other four spent four weeks at Duke and six weeks at the European Center for Nuclear Research (CERN) near Geneva, Switzerland, working on particle physics projects. Having the nuclear and particle physics students in the same program facilitated cross-field intellectual exchange and the sharing of resources needed by both groups, while the participation of the Duke high energy physics group in the program gives it an international component.

Through introductory lectures and direct research involvement, the students gain experience and insights in the main stages of scientific research in nuclear and particle physics:

- The development of concepts to probe specific features of nuclear matter, particles and fields;
- The design, construction, testing, and installation of equipment and instrumentation;
- Data acquisition, analysis, and interpretation; and
- The dissemination of research results.

In addition to direct involvement in research projects, the REU program at Duke includes activities that are designed to broaden the students' physics foundation, enhance their research skills, and build confidence. These activities include: (1) regular meetings with the program coordinator, (2) research tutorials and special topic lectures, (3) a science writing tutorial, and (4) a required report and presentation by each student at the end of the program. The research reports written by the students form the main body of this document.

Personnel

2024 TUNL REU Participants

Student	*Home Institution*	*Faculty Advisor(s)*	*Class*
Phoebe Alva Rosa	Augsburg U.	Forrest Friesen	Soph
Kwame Bennett	Haverford College	Ashutosh Kotwal	Jr
Lilla Carroll	Mount Holyoke College	Caleb Marshall	Jr
Sarah Estupinan Jimenez	Montclair St U.	Jingyi Zhou	Jr
Matthew Gratrix	U. Connecticut	Ayana Arce	Jr
Celeste Guerrero	U. of the Pacific	Kate Scholberg	Soph
Jordan McPherson	Longwood U.	Danula Godagama	Jr
Keegan Mencke	Lawrence U.	Anselm Vossen	Jr
Grace Miller	Cleveland State U.	Mark Kruse, Ayana Arce	Soph
Thomas Ordahl	St. John's U. (MN)	Sean Finch	Jr
Penn Smith	Lebanon Valley College	Anselm Vossen	Jr
Khushi Vandra	Villanova U.	Mark Kruse, Ayana Arce	Soph
Thomas Waterman	U. of Dallas	Alexander Crowell	Soph

2024 TUNL REU Administration

Principal Investigator and Program Director:
Dr. Alexander Crowell

Co-Principal Investigator and CERN Experience Director:
Professor Ayana Arce

Participants in the 2024 TUNL Research Experiences for Undergraduates (REU) program. Shown in the photograph from left to right are: (front row) Phoebe Alva Rosa (Augsburg University), Sarah Estupinan Jimenez (Montclair State University), Lilla Carroll (Mount Holyoke College), Grace Miller (Cleveland State University), Jordan McPherson (Longwood University), Penn Smith (Lebanon Valley College); (back row) Celeste Guerrero (University of the Pacific), Khushi Vandra (Villanova University), Keegan Mencke (Lawrence College), Thomas Ordahl (St. John's University - MN), Thomas Waterman (University of Dallas), Kwame Bennett (Haverford College), Matthew Gratrix (University of Connecticut).

Research Based at Duke

Chapter 1

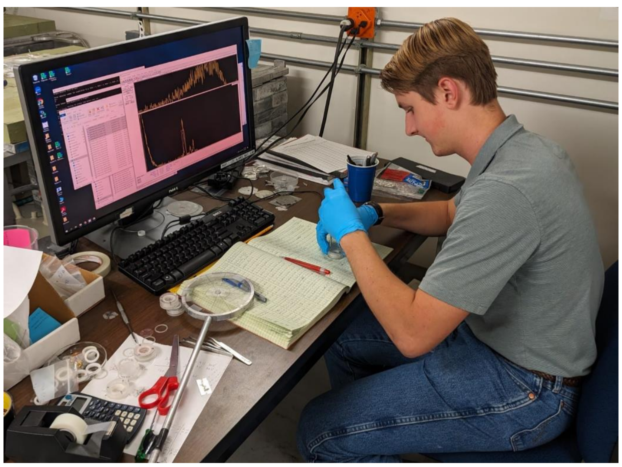

1.1 A GPU-based Data Acquisition System for Compton Experiments at HIγS

J. McPherson, *Longwood University, Farmville, VA*; D. Godagama, *TUNL*

Background The Compton@HIγS collaboration measures neutron polarizabilities by performing Compton scattering experiments on light nuclear targets. The HIγS data acquisition system (DAQ) consists of ten CAEN V1730 waveform digitizers that digitize the complete pulse shape of more than 100 signal channels from an array of NaI detectors. The data is transferred from the digitizers to a VME controller, and then to the DAQ computer for data processing.

Purpose The purpose of this project was to install a GPU inside the DAQ computer and utilize modern GPU parallel programming techniques to increase data processing speed for all future Compton@HIγS experiments.

Methods Several programs were written to test the performance of the NVIDIA T1000 GPU after installation. Using the CUDA parallel computing platform by Nvidia Corporation, steps were taken to optimize computing techniques necessary for raw data processing.

Results The GPU was found to be 51% faster at performing the same function in parallel as was performed serially on the CPU. A parallel reduction code was optimized to understand CUDA performance characteristics and how to achieve peak bandwidth. Several example CUDA programs were written that perform precise timing and energy measurements for raw waveform processing.

Conclusions Once additional programs are optimized for peak GPU performance, they will be stored in a programming library accessible for offline data processing at HIγS.

I. Introduction

The High Intensity Gamma-ray Source (HIγS) facility is located in the Duke Free Electron Laser Laboratory and operated by the Triangle Universities Nuclear Laboratory (TUNL). Compton experiments at HIγS study the neutron's internal structure using Compton scattering on light nuclear targets such as hydrogen, deuterium, and helium. Previously, a CPU-based data acquisition system (DAQ) digitized and preserved the complete waveforms of over 100 signal channels from several NaI detectors (see Fig. 1.1). When an experiment is running, we collect about 2 TBs of data every day. Processing that much data is computationally demanding, and although our previous CPU-based DAQ performed effectively, we wanted to utilize the power of modern GPU programming techniques to increase data processing speed.

The HIγS DAQ consists of ten CAEN V1730 16-channel, 14-bit 500 MS/s FLASH ADC Waveform Digitizers that process entire pulse shapes through analog-to-digital converters (ADC's). These pulses are written in circular memory buffers that allow data acquisition to continue with negligible dead time. All digitizers are synchronized to a common clock to ensure Trigger Time Stamps alignment and that data corresponds to the same event. Data is then transferred to a STRUCK SIS3153 VME controller via the VME bus back panel connection. The VME64/VME64X interface has a data transfer rate of up to 150 MB/s. The data is finally transferred to a DELL R540 server via a USB 3.0 connection with an average transfer speed of 250 MB/s. DAQ software writes this unprocessed data into binary files that can be read by a C++/ROOT program for offline analysis [God22]. This program performs charge integration (QDC) and constant fraction discrimination (CFD) on raw pulses to determine energy deposition and precise time measurements. Although currently this program runs on the CPU, some of the raw data processing can be parallelized and performed on a GPU.

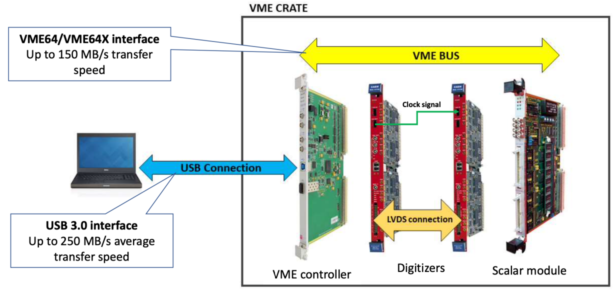

Figure 1.1: Layout of the DAQ system [God20].

The main difference between a CPU and GPU amounts to their different processing capabilities. From a hardware perspective, the Central Processing Unit (CPU) has a few cores and dedicates a greater area to its control units and memory caches. This allows the CPU to perform a variety of computing tasks from complex calculations to the basic commands that run your computer and operating system. The Graphics Processing Unit (GPU) contains hundreds of cores with smaller control and cache sizes. Because of its decreased control and cache area, the GPU cannot perform overly complex operations like the CPU. However, its hundreds of cores allow the GPU to perform massively parallel calculations, making it ideal for processing large amounts of data. In general, we use the CPU for tasks requiring serial processing, and the GPU for parallel processing. Because much of our raw data processing at HIγS requires performing the same calculations on thousands of pulses, we can compute on the GPU to increase our processing efficiency.

II. Methods

After the NVIDIA T1000 GPU was installed in the DAQ server, we ran `deviceQuery` to see the properties of the GPU. The NVIDIA T1000 GPU uses CUDA Driver Version 12.2 and CUDA Runtime Version 12.0. The total global memory on this GPU was 3904 Mbytes. For each of its 14 multiprocessors the GPU had 64 CUDA cores for a total of 896 CUDA cores. Parallel processing was achieved by launching multiple threads and thread blocks, where each thread performs the same operation simultaneously. The maximum number of threads per block was 1024. CUDA functions, called kernels, launch multiple blocks and hundreds of threads to perform massive parallel computations.

The initial goal was to write simple parallel processing programs utilizing the various specifiers and memory allocation calls from the CUDA Toolkit. NVIDIA Distinguished Engineer Mark Harris wrote several articles on CUDA techniques, including an introductory piece on how to use CUDA [Har17]. In CUDA, a kernel is a function that uses the `__global__` specifier, allowing the function to be called from the CPU and run on the GPU. In launching the kernel, the number of blocks and threads/block must be specified: `kernel<<<blocks, threads>>>(inputs)`. To compute on the GPU, memory must be allocated that the GPU can access. There are several calls, such as `cudaMalloc` and `cudaMallocManaged` that allocate GPU-accessible memory. At the end of `main()`, the allocated memory is freed by using `cudaFree`.

Two important tasks performed on raw data are QDC and CFD. The energy deposition is proportional to the total charge, determined from integrating a raw data pulse. CFD is a method used to produce more precise timing information. Triggering from a fixed threshold results in timing jitter because different pulses reach different amplitudes. Two sample programs were written to perform QDC and CFD on random 2000 element arrays.

To perform charge integration, CUDA parallel reduction was optimized for peak GPU performance. Parallel reduction utilizes parallel processing techniques to compute the sum of all elements in an array. For an array of 2000 elements, the first reduction utilized 8 blocks and 256 threads each. Reduction was achieved by assigning a single thread to add two neighboring elements and depositing them back into the array, then repeating this step with half the number of threads until the sum was reached. The local reduction computed the sum of each block, then the global reduction (using only 1 block and 8 threads) computed the final sum. Mark Harris outlined several optimization techniques to ensure that CUDA parallel reduction runs efficiently and achieves peak memory bandwidth [Har24].

Instead of using CFD-based hardware, such as an electronic processing device, raw data pulses are stored in binary files that can be read and processed offline. Therefore, CFD was performed on an array of 2000 elements using parallel processing techniques. The first step in performing CFD was to create an array that was the inverse of the raw pulse array with some delay. Then, the raw pulse and inverted, delayed pulse were added together to get the CFD pulse (shown in Fig. 1.2). The precise timing measurement was determined by calculating the zero crossing point. To do so in CUDA, the concept of parallel reduction was applied to find the minimum and maximum. Instead of having one thread deposit the sum of two elements, the thread deposits either the greater than or less than element. By modifying the reduction technique, the "x" and "y" min and max values were found and used to calculate the zero crossing point based on similar triangle geometry. Timing information obtained by performing CFD will be used in later analysis to determine time of flight.

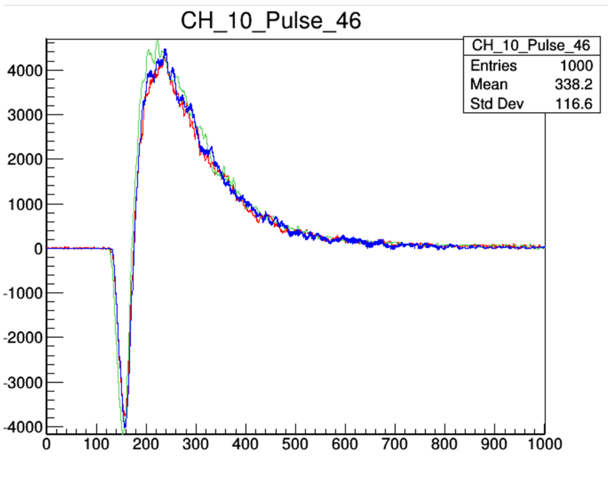

Figure 1.2: CFD pulses from several channels (processed on the CPU).

III. Results

In a sample program adding arrays of two hundred million elements, the addition function was found to be 51% faster on the GPU than CPU. The `gprof` profiler was used to obtain timing information for the C++ based CPU program, and `nvprof` was used for CUDA program. The CPU function took 666.33 ms while the GPU kernel took 441.17 ms. These simple profiles demonstrated the efficiency of the GPU in processing large datasets, such as the ones received from the HIγS DAQ.

A QDC, or charge integration, program was written that wrapped the functions and kernels into a single executable function that can be called from the CPU. The same was done for the CFD program. Both of these programs were optimized to account for memory coalescing, divergent branching, bank conflicts, and latency hiding. Optimizations included using sequential thread addressing and other CUDA techniques outlined by Mark Harris. These programs do not currently process raw data, but are the first step in developing a library or libraries for use in Compton@HIγS data processing.

IV. Conclusions

Although the hardware was installed and sample programs were written, no data processing was carried out on the GPU. Before processing with raw pulse data can begin, the programs must be modified to access and read the binary files stored by the DAQ software. Additionally, the timing and energy information obtained by performing QDC and CFD must be written into a ROOT tree for further analysis.

In addition to editing the QDC and CFD programs for true raw data processing, these programs must be further optimized. Based on the workload and transfer demands, these programs should be adjusted to consider the different performance implications of `cudaMallocManaged` and `cudaMalloc`. Currently, the programs use `cudaMallocManaged` for memory allocation. Because `cudaMallocManaged` allocates Unified Memory accessible by both the CPU and GPU, it is better for optimizing data transfers, but not performance. `cudaMalloc` allocates memory only on the GPU and provides better performance for GPU computations by avoiding the overhead from memory coherence between the CPU and GPU. Because most of the data processing at HIγS can be performed in parallel on the GPU with minimal data transfers, using `cudaMalloc` should improve the performance of the programs. The CUDA profiler, `nvprof`, can be used to compare the performance between the two memory allocation calls. Additionally, the profiler should be used to inspect memory usage and transfer time, kernel execution time and launch metrics, occupancy, and other performance metrics. Once the QDC, CFD, and additional programs are optimized for peak GPU performance, they will be wrapped and stored in a programming library accessible for offline data processing at HIγS.

[God20] D. Godagama, *Kmax-based data acquisition system for HIγS*, 2020, Presentation.

[God22] D. Godagama, Ph.D. thesis, University of Kentucky, 2022.

[Har17] M. Harris, *An Even Easier Introduction to CUDA*, 2017, NVIDIA Technical Blog.

[Har24] M. Harris, *Optimizing Parallel Reduction in CUDA*, 2024, CUDA Webinar.

1.2 Cosmic Study for Compton Scattering Measurements at HIγS

S. Estupinan Jimenez, *Montclair State University, Montclair, NJ*; J. Zhou, *TUNL*

The COMPTON@HIGS collaboration is working to understand how nucleons respond to external electromagnetic fields due to their internal structure and the nature of the nuclear strong force. This is done by inducing Compton scattering between gamma rays with energies in the range of 60–100 MeV and different types of light nuclei. Currently, a liquid ^{3}He target is being used to study the neutron, and the experiment is running at the High Intensity Gamma-ray Source (HIγS) Facility. To conduct such measurements successfully, background suppression, especially from cosmic rays, is important. In this project, a new veto paddle was developed to further reduce background events in data collected by the five NaI detectors (HINDAS). The typical cosmic rate in a HINDA detector is around 72,000 counts per hour. With a series of preexisting methods, we could reduce the rate to nearly 50 counts per hour. With the paddles, we further reduced the background by a factor of two, bringing the signal-to-noise ratio closer to 1:1.

I. Introduction

The COMPTON@HIGS collaboration focuses on understanding the internal structure of nucleons by gathering more information on the cross section of the neutron through Compton scattering. Compton scattering is the interaction between a photon and a charged particle. The collaboration is focusing on using light nuclei (A = 1–6) with photons of different energies. The current experiment uses liquid ^{3}He as a target and 100 MeV gamma-ray photons to probe nuclei at HIγS.

A significant challenge for this program arises due to the high energies of the γ rays. The energy of the Compton signal is very close to the one deposited by some cosmic rays, and the shielding system of the HINDA detectors is less effective at these high energies. Additionally, some out-of-plane detectors are not effectively shielded from cosmic rays due to their placement. The shields work to remove any signals that are not coming directly from the target. Part of the core of the in-plane HINDA detectors is also uncovered. This necessitated the development of new detectors, or paddles, to be mounted on top of the HINDA detectors to further reduce the cosmic background signal. A drawing of the experiment setup is shown in Fig. 1.3.

II. Methods

The veto paddles are composed of a thin scintillating sheet, a cylindrical light guide, a photo-multiplier tube (PMT) covered in reflective material, and a tarp to prevent light leaks (see Fig. 1.4). The goal of this project was to test and mount these paddles onto the HINDA detectors within the limited timeframe between experiments at 60 MeV and 100 MeV. Testing the six paddles involved addressing any light leaks and determining the optimal operating voltage for the detectors. Given that most PMTs were different models, their performance was not fully characterized. A properly functioning paddle would exhibit a clear separation between low-energy counts and the actual cosmic peak in a histogram (see Fig. 1.5). This separation is critical, as the position of the peak is used to apply energy cuts and implement the veto paddle during data analysis.

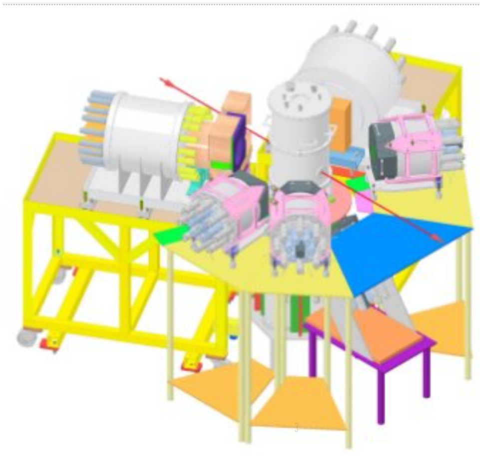

Figure 1.3: Target and detector setup

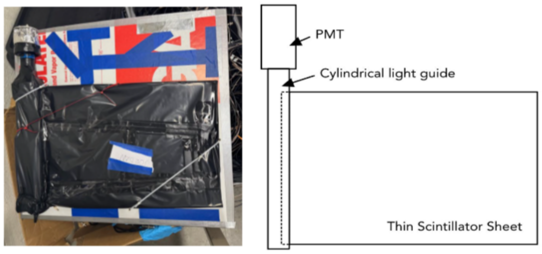

Figure 1.4: Schematic of the paddle design along side a photo of a constructed veto detector.

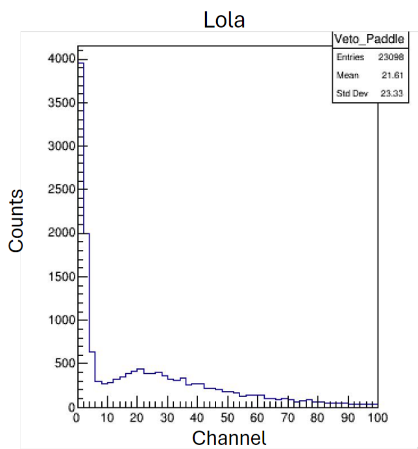

Figure 1.5: Uncalibrated energy spectrum from one of the paddle detectors.

The next step was to mount the paddles onto the HINDA detectors. We utilized existing screw holes in the detector frames for mounting. The supports had to be stable, lightweight, and non-intrusive to allow the team to continue their work in the area without obstruction (see Fig. 1.6). This design makes mounting and dismounting the paddles easy as well as facilitating their alignment. After mounting the paddles, we added an additional layer of protection against light leaks by covering all detectors with aluminum foil.

III. Results

The performance of each veto paddle varies, requiring individual analysis of the data collected from each one, considering variables such as placement and surrounding materials. We determined the optimal operating voltages for each paddle and mounted them in the experiment setup (see Fig. 1.7). Preliminary data analysis revealed that even our least effective HINDA detector achieved a 50% reduction in the cosmic signal due to the veto paddle. This result is promising, indicating that the other paddles are likely to perform even better.

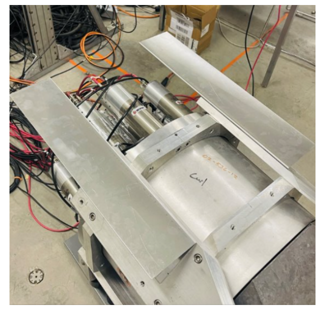

Figure 1.6: Mount for paddle on in-plane detectors

The primary challenge in our experiment is the high rate of cosmic signals, which occur at approximately 72,000 counts per hour. In contrast, the Compton signal is much weaker, registering around 20 counts per hour. To address this, several methods are employed to significantly reduce the cosmic signal rate. The most critical technique is the time-of-flight cut, which leverages timing information from the accelerator and correlates it with detector data. Since photons are emitted in pulses, this method allows us to exclude any data collected outside the relevant time window, reducing the cosmic signal rate by approximately 97%. Another key method is the energy cut. By filtering the data based on the known energy range of the expected Compton signal, we can eliminate 90% of the remaining cosmic data. Additionally, the shielding system around the detectors further decreases the cosmic signal survival rate by 23%. Despite applying these cuts, the ratio of cosmic signals to Compton signals remains 2:1. To minimize the uncertainty in our experiment, paddles are used to reduce the background signal by a factor of two or more, which is essential for maintaining the accuracy of our results.

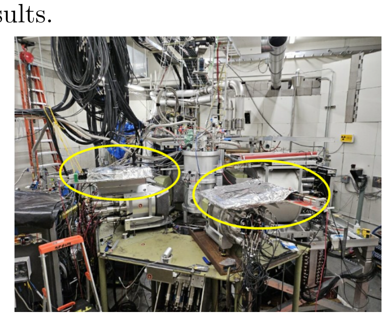

Figure 1.7: Photo of experimental setup with new veto paddles circled.

IV. Conclusions

The paddles as shown on Fig. 1.7 have been mounted and tested. They can be used for similar experiments that require extra efforts for cosmic background reduction. The mounts for the paddles use the structure of the detectors, which allows for practicality and efficiency.

1.3 Construction and Commissioning of a Cryogenic Silicon Detector Test Chamber and Beam Line for Proposed DRad Experiment

P. Alva Rosa, *Augsburg University, Minneapolis, MN*; F.Q.L. Friesen, *TUNL*

Background The deuteron is the only bound two-nucleon system, and as such, it is fundamental to know its properties to high degrees of accuracy. At very low momentum transfer, the electromagnetic properties of the deuteron, such as rms charge radius, can be predicted using theoretical models. The rms charge radius is thus a strong candidate for comparisons between experimental results and theory.

Purpose Recommission the 59° beam line in TUNL's Tandem Laboratory in order to test the efficiency of silicon solid state particle detectors operating under cryogenic temperatures in support of proposed measurements of the deuteron rms charge radius at Jefferson Lab.

Methods Expose the detectors to α particles from a ^{241}Am source. The beam line is capable of delivering proton and deuterium beam to target, where they are scattered off of a thin gold foil into a Silicon Barrel Detector and Silicon Strip Detector (SSD). The SSD was mounted directly onto the exposed cold head of a cryo-cooler using an aluminum mounting plate in order to optimize thermal contact.

Results The 59° beam line was successfully recommissioned and a test chamber with cryogenic capabilities was constructed. A direct correlation between the temperature and detector leakage current was measured. Initial detector characterizations were performed.

Conclusions Decreasing the temperature of the SSD and Barrel detector also decreases the leakage current. This helps minimize the noise seen by the detectors. A full accelerator run will be necessary to finish the detector characterization. This chamber will allow for R&D of detector assemblies at temperatures significantly lower then typical applications.

I. Introduction

There are two principal ways to determine the rms charge radius of light nuclei: elastic electron scattering and laser spectroscopy. Historically, the results produced using these two methods were consistent within experimental uncertainties. This agreement led researchers to combine results into the world average values for proton (r_p) and deuteron (r_d) charge radius that was published in the CODATA compilations [Moh10].

Recently, ultra-precise measurements of muonic atoms resulted in r_p and r_d values inconsistent with those produced by CODATA. Notably, the r_p value found using spectroscopy of muonic hydrogen had a 7 σ discrepancy from the CODATA value. This brought about the Proton Size Puzzle that was investigated in the Proton Radius (PRad) experiment at Jefferson Lab. A similar, about 6 σ, discrepancy in the r_d value was found from laser spectroscopy of muonic deuterium but the idea of a subsequent Deuterium Size Puzzle was initially dismissed owing to the fact the the r_p and r_d values were highly correlated. However, recent reanalysis of spectroscopy data of anatomic deuterium resulted in a r_d value with a 3.5 σ discrepancy from one reported by CODATA. This value was found independently of r_p and has confirmed the existence of a Deuterium Size Puzzle shown in Fig. 1.8.

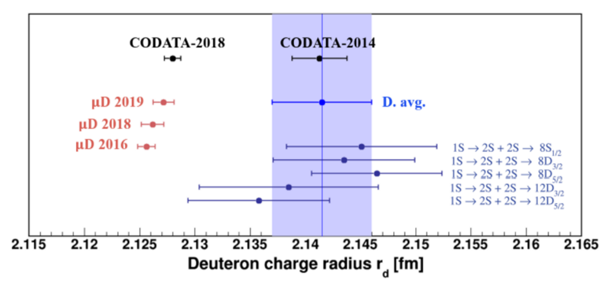

Figure 1.8: r_d values reported by various papers demonstrating deuteron rms charge radius discrepancies [Bul23]

Similar to the aforementioned PRad experiment, Jefferson Lab has proposed a Deuterium Radius (DRad) experiment. It will be performed using an upgraded version of the PRad experimental set up with a couple alterations. These include a windowless gas flow deuterium target instead of hydrogen and a Silicon Strip Detector (SSD). Because the gas flow target will be operated at 20K, it is of high importance to have a comprehensive understanding of how the efficiency and resolution of the SSD are affected by operating under cryogenic temperatures. TUNL's Tandem Laboratory will be used to test the detector efficiency for protons and deuterons in the 1 - 10 MeV range.

II. Methods

A. Silicon Detectors

Silicon detectors are solid state detectors that are created using two wafers of differently doped Si, n-type and p-type. A mechanical connection is made between the n-type and p-type Si which causes free electrons and holes to recombine and establishes a depletion region within the detector. The detector is then reverse biased in order to increase the size of the depletion region and provide this region with an electric field that helps remove charge carriers caused by incident particles [Poo10]. The equation for full depletion voltage (V_{fd}) is given as:

$$V_{fd} = q2\epsilon_0\epsilon_s * D^2 * \mid N_{eff} \mid$$

with ϵ_0 as the permittivity of free space, ϵ_s as the permittivity of silicon, D as the effective doping density, and N_{eff} as the detector thickness [Col00].

Signals are generated by charged particles traversing the depletion region within a detector. As these particles move through the depletion region, they ionize electron hole pairs which creates a current that can be read out by electrodes. Because the amount of energy required to excite an electron hole pair is known (3.6 eV), measuring the number of electron hole pairs allows the energy of the incident particle to be determined [Kno10].

One factor that can be detrimental to good signal resolution is leakage current or current caused by minority charge carriers within the depletion zone. For n-type and p-type doped Si, the minority charge carriers are holes and electrons respectively. Because Si detectors rely on current readings to output data, these minority charge carriers can flood the signal with noise and make getting a spectrum challenging. One way to mitigate the effects of leakage current is to operate Si based detectors at cryogenic temperatures. This is because at low temperatures, thermal excitation of electrons into the conduction band is greatly reduced which results in fewer thermally generated charge carriers that create current.

B. Experimental Setup

In order to begin detector characterization, the 59° beam line in the tandem accelerator facility needed to be recommissioned. This involved installing multiple sections of 2" beam pipe to the preexisting beam line, attaching necessary hardware to ensure the beam was steered and aligned correctly, and ensuring proper vacuum was obtained along the entire length of the beam line. Additionally, a vacuum test chamber was designed and commissioned to assist future research at TUNL involving detector operation at cryogenic temperatures.

Gaps in the beam line in both the high energy bay and target room one (TR1) were resolved with the addition of multiple segments of 2" dependex beam pipe (see Fig. 1.9). Steerer magnet S5 in TR1 was also added to increase steering capabilities and ensure it's possible to get beam on target. Two gate valves, one on either side of the test chamber were introduced to ensure vacuum isolation from the rest of the beam line. This allows the chamber to be vented to atmosphere without interfering with the downstream vacuum.

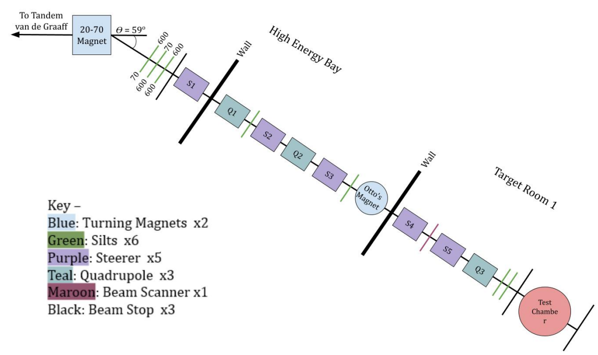

Figure 1.9: Schematic of 59° beam line upstream of 20-70 turning magnet

A combination of both roughing and high-vacuum pumps were used to create four individual vacuum systems along the beam line and within the detector chamber. Beam pipe and chamber hardware were connected using a combination of dependex and flange vacuum fittings that rely on rubber o-rings to create a leak-free mechanical connection. Rotary vane roughing pumps were then used to reach a roughing pressure on the order of 1×10^{-1} torr, at which point a turbomolecular pump is engaged in order to obtain an ultimate pressure of $\sim1\times10^{-6}$ torr.

It's often necessary to leak chase various components of the beam line in order to identify and resolve leaks that prevent good vacuum. For this project, both a MS-40 and Alcatel ASM 120h leak detector were used to monitor the leak rate and pinpoint leaks across the entire setup. Leak detectors vary slightly machine to machine, however the basic modality remains consistent. A leak detector device is connected to the vacuum system being leak chased, then—depending on the size of the system—it is pumped down using only the leak chasers internal pump or and external roughing pump. Helium is sprayed on the outside of the test set up. If a leak is present, the He will enter the vacuum system, flow into the leak chaser, and be detected by an internal mass spectrometer. This will cause the leak rate and pressure displayed on the leak chaser to spike, demonstrating there is a leak in the sprayed location.

A preexisting vacuum test chamber was recommissioned to assist with the characterization of Si detectors for the Jefferson Lab DRad experiment and future research at TUNL. The exposed cold head from a cryo-cooler was mounted directly onto the chamber exterior and protrudes slightly into the chamber. This allows detectors and other hardware to be mounted directly onto the cold head. In order to mount the chamber, two custom flanges were designed in CAD and machined using a lathe and drill press. Both flanges converted non-standard bolt spacing to 4" dependex pipe. Additionally, a Faraday cup was installed as a beam stop to monitor the current produced by the beam.

Internally, an Al mounting plate was attached to the end of the cold head. A 500 μm thick Silicon Strip Detector (SSD) was then mounted onto the Al plate in order to maximize thermal contact. A 40 μm thick Si Barrier Detector (SBD) was placed in front of the SSD with a collimating nose pointed directly at a Au foil target. The SSD and SBD were biased to 350 V and 30 V, respectively. The SSD was read out using a Mesytech VMMR module while the SBD used a MDPP module. The DAQ was controlled using a MVLC VME controller. A ^{241}Am α source was installed off to the side of the SSD in order to assist with detector calibration (see Fig. 1.10).

III. Results

The commissioning of the 59° beam line was considered officially completed on July 17, 2024 when 25nA of 12 MeV proton beam reached the beam stop directly before the test chamber. Due to time and accelerator constraints, we were unable to get beam on target and make initial e-d elastic scattering measurements.

Additionally, the SBD was cooled down to 75 K and a spectrum from a ^{241}Am α source that matched the typical de-excitation pattern was seen, see Fig.1.11. The leakage current within the SBD was also monitored as the cold head was cooled and a significant drop in current was seen. Due to limitations of the readout device,it was difficult to track the exact current value below 100 K.

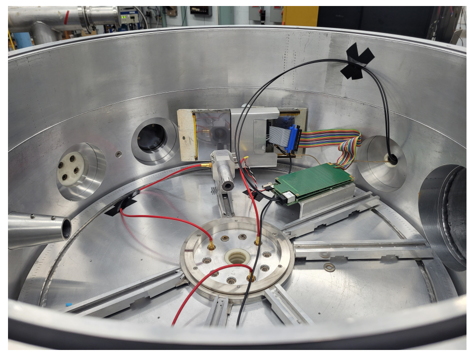

Figure 1.10: Layout of Si detectors inside the modified test chamber

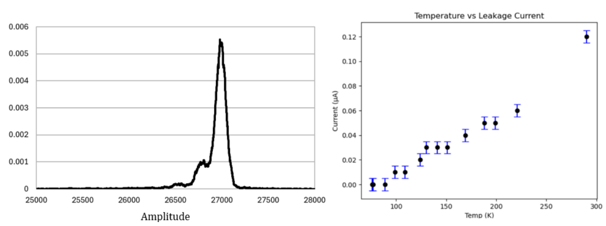

Figure 1.11: Spectrum from ^{241}Am source (*left*) and a graphic illustrating the relationship between leakage current and temperature (*right*)

IV. Conclusions

Major steps towards accurate calibration of Si detectors operating at cryogenic temperatures have been made in support of Jefferson Lab's proposed DRad experiment. A correlation between detector temperature and leakage current rate was found within 0.005 μA, however it may be necessary to procure a more precise readout module to decrease this uncertainty.

The 59° beam line is now fully operational and can be used for SSD calibration runs with 1-10 MeV proton and deuteron beams as well as future R&D at the Tandem Laboratory. In order to cool the detectors down to the temperatures proposed by DRad, it may be necessary to attach the cold-head to a compressor with more cooling power then the one currently in use and improve the thermal connections between components.

[Bul23] D. Bulumulla *et al.*, Experimental proposal submitted to Jefferson Laboratory, (2023).

[Col00] P. Collins *et al.*, Nucl. Instrum. Methods, **A447**, 151 (2000).

[Kno10] G. F. Knoll, *Radiation Detection and Measurement*, John Wiley and Sons,, 5th edition, 2010.

[Moh10] P. J. Mohr, B. N. Taylor, and D. B. Newel, J. Phys. Chem. Ref. Data, **41**, 043109 (2010).

[Poo10] O. Pooth, *The CMS silicon strip tracker: Concept, production and commissioning.*, Springer Science and Business Media, 2010.

1.4 Reaction Cross Sections for ^{191}Ir(n,2n)^{190}Ir and ^{193}Ir(n,2n)^{192}Ir

T. Waterman, *The University of Dallas, Dallas, TX*; A.S. Crowell, *TUNL*

Background Iridium was used as a neutron fluence monitor during underground nuclear tests. Due to this historical use, it is imperative for the scientific community to have a good understanding of the nuclear properties, specifically the various cross sections of the two stable isotopes of iridium.

Purpose Currently, near the low energy threshold of the (n,2n) cross section for both ^{191}Ir and ^{193}Ir, the uncertainty on the cross sections value is around 30 percent [Cha07]. By accurately and precisely measuring the (n,2n) cross section in this region, the experiment seeks to drastically reduce the uncertainty in the cross section.

Methods The TUNL tandem accelerator was used to irradiate natural iridium foils with several mono-energetic neutron beam energies ranging from 8.0 MeV to 13.5 MeV. After exposure to the neutron beam, the gamma-ray decay spectrum of the iridium target was acquired using HPGe detectors.

Results Using the spectral data from the HPGe detectors, the cross section for the (n,2n) reaction was calculated.

Conclusions Overall, the cross section for the ^{191}Ir(n,2n)^{193}Ir reaction agreed with the ENDF B-VIII.0 prediction up to 12 MeV. At this point, the calculated cross section was below the ENDF line, in agreement with most other experiments. The ^{193}Ir(n,2n)^{192}Ir reaction cross section agreed well with both the ENDF prediction as well as other experimentally determined points.

I. Introduction

Iridium has uses and applications across many fields including nuclear medicine and high-temperature industry applications. During underground nuclear tests in the 1950's, iridium, a very dense metal, was used to measure neutron fluence. Over many years, various groups have measured the (n,2n) cross section of the two natural isotopes,^{191}Ir and ^{193}Ir. Most of these measurements have been focused in the 13–16 MeV range. At this energy range researchers found that the cross section appeared relatively constant, like a plateau. Additionally, several measurements were made at higher energies where the (n,2n) cross section begins to decrease as the (n,3n) reaction is favored. Finally, only a handful of measurements have been made from the threshold of the (n,2n) reaction to the plateau region. This lack of data in the low energy region led researchers to ascribe up to a 30% uncertainty to the ENDF theoretical cross section [Cha07]. The data on the (n,2n) cross section prior to this experiment is shown in Figures 1.12 and 1.13 [Cha07, Bay75, Her84, Kal18, Kal19, Pat07, Vla17, Qai72, Vla07, END11].

In order to assist the scientific community in understanding the (n,2n) cross section, this experiment sought to experimentally determine the cross section from 8.0 MeV up to the plateau region of 13.5 MeV. The cross section would be measured in 0.25 MeV increments from 8.0 MeV to 9.5 MeV and in 0.5 MeV increments until 13.5 MeV. Due to the large amount of data points measured compared to the relatively few iridium foils available for exposures, it has taken several summers to perform all the runs at various energies as well as then waiting for the foil to decay back to its ground state. The earliest set of runs were performed in June 2017 and the most recent set of runs were performed in June 2024.

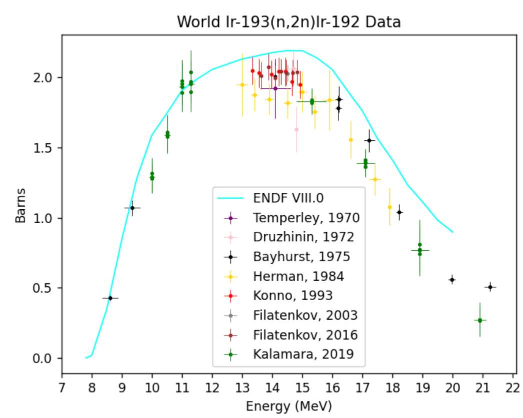

Figure 1.12: World ^{193}Ir(n,2n)^{192}Ir Data

^{193}Ir(n,2n)^{192}Ir

The heavier natural isotope of iridium has a natural abundance of 62.77%. According to ENDF VIII, ^{193}Ir(n,2n)^{192}Ir has a threshold of 7.813 MeV

[END11]. This reaction results in a ^{192}Ir nucleus with a 73.862 day half-life and undergoes β-decay. This decay produces many different characteristic gamma rays that may be seen in a HPGe detector. Due to their high intensity, this experiment analyzed the 316 keV and the 468 keV gamma rays.

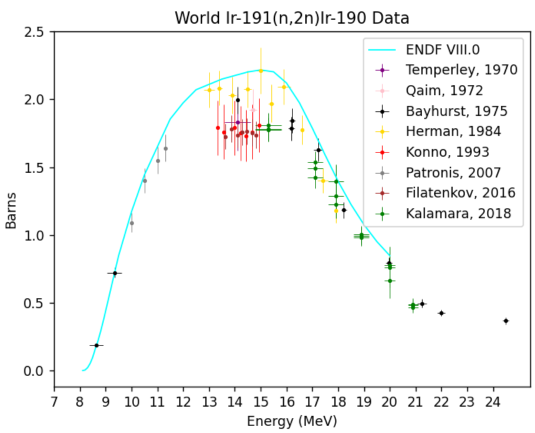

Figure 1.13: World ^{191}Ir(n,2n)^{190}Ir Data

^{191}Ir(n,2n)^{190}Ir

The lighter isotope of iridium, according to ENDF VIII has a threshold of 8.115 MeV for the (n,2n) reaction [END11]. The ^{190}Ir nucleus has a half life of 11.78 days. Similarly to the ^{192}Ir nucleus the ^{190}Ir nucleus as it decays emits many different characteristic γ rays. The 518 keV and the 558 keV gamma rays were analyzed to determine the cross section as they have a large intensity and form excellently resolved peaks. For instance, the 511 keV peak from electron-positron annihilation was quite distinct from the 518 keV ^{190}Ir peak.

II. Methods

In order to probe the cross section at very specific energies, the TUNL tandem accelerator was used. To eventually produce mono-energetic neutrons, a deuterium beam was first generated through the DENIS II Source. Then, by utilizing a feedback loop between the 20-70 magnet, which bends the beam into the desired beam line, and the accelerating potential, the energy of the deuterium beam becomes very precise and well known. Finally, the deuterium beam is guided into a deuterium gas cell causing the following reaction to occur: D(D,n)^{3}He. The unique setup at the tandem allowed the experiment to create a nearly mono-energetic beam of neutrons at the desired energy $\pm$30 keV. After irradiation, the iridium and monitor foils were transported to the low-background counting facility where they were placed at a distance of 5 cm away from a HPGe detector. Once the spectra were gathered, a software called GoodFit was used to integrate over the peaks to determine the number of counts corresponding to each characteristic gamma ray [Goo15]. Then the following equation was used to calculate cross section:

$$\sigma = \frac{A}{\phi n(1 - e^{-\lambda t_i} e^{-\lambda t_d}(1 - e^{-\lambda t_m})}$$

σ	Cross Section
A	Activity
ϕ	Neutron Flux
n	Number of Target Nuclei
t_i	Irradiating time
t_d	Decay Time
t_m	Measurement Time

III. Results

Overall, the results of this experiment agreed well with the ENDF prediction line. Interestingly, all the measured values for the cross section of both isotopes were slightly below the cross section proposed by ENDF and this discrepancy became larger as the plateau region was approached. This discrepancy in the ENDF line seems to stem from the heavy reliance of the ENDF prediction on Herman's data from 1984 rather than all the other published measurements. This deviation was most noticeable in the ^{191}Ir(n,2n)^{190}Ir reaction where this experiment's values for the cross section, in agreeing with most other experimentally determined points, suggested a plateau region with a lower cross section. This trend is shown in Figure 1.14 and 1.15 [Cha07, Bay75, Her84, Kal18, Kal19, Pat07, Vla17, Qai72, Vla07, END11].

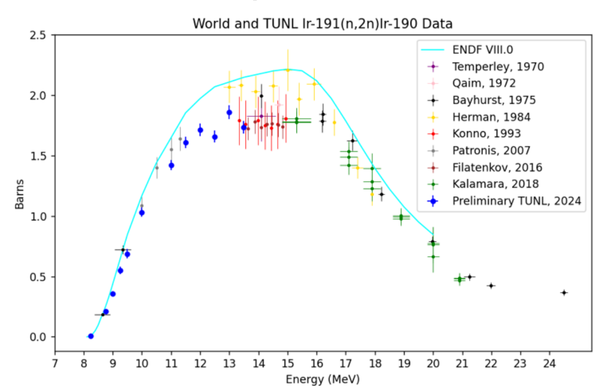

Figure 1.14: World and TUNL ^{191}Ir(n,2n)^{190}Ir Data

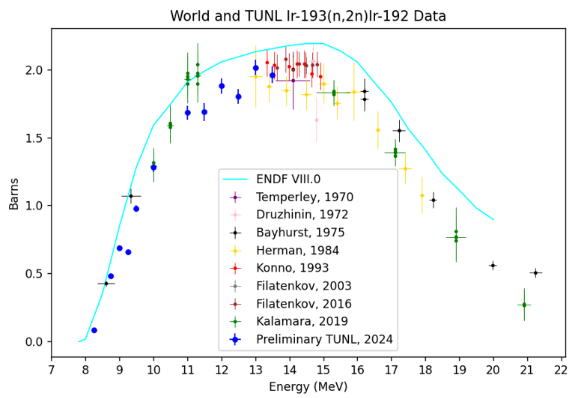

Figure 1.15: World and TUNL ^{193}Ir(n,2n)^{192}Ir Data

For each isotope, two prominent characteristic gamma rays were analyzed. The final reported cross section was obtained by averaging the cross sections from the two different gamma rays. For the ^{193}Ir(n,2n)^{192}Ir isotope, both the 316 keV and the 468 keV gamma rays resulted in extremely similar cross sections. On the contrary, the 518 keV and the 558 keV gamma rays from the ^{191}Ir(n,2n)^{190}Ir reaction, in nearly every run, resulted in the 518 keV line showing a slightly lower cross section and the 558 keV showing a slightly larger cross section. This is potentially due to slightly incorrect intensities in the NuDat 3.0 database, where this experiment obtained the expected intensities of the gamma rays [Nu224]. The numerical cross section data determined by this experiment is shown below:

Table 1.1: ^{193}Ir(n,2n)^{192}Ir Cross Section Data

Energy (MeV)	Cross Section (barns)	Uncertainty (barns)
8.00	0.01074	0.00035
8.25	0.0838	0.0091
8.75	0.4799	0.0121
9.00	0.6885	0.176
9.25	0.6572	0.0168
9.50	0.9772	0.0250
10.0	1.2841	0.0390
11.0	1.6835	0.0513
11.5	1.6877	0.0666
12.0	1.8795	0.0570
12.5	1.8000	0.5434
13.0	2.0126	0.0608
13.5	1.9607	0.05927

Table 1.2: ^{191}Ir(n,2n)^{190}Ir Cross Section Data

Energy (MeV)	Cross Section (barns)	Uncertainty (barns)
8.25	0.0067	0.0004
8.75	0.2129	0.0124
9.00	0.3560	0.0208
9.25	0.5493	0.0321
9.50	0.6879	0.0400
10.0	1.0314	0.0395
11.0	1.4221	0.0435
11.5	1.6106	0.0488
12.0	1.7120	0.0521
12.5	1.6580	0.0503
13.0	1.8597	0.0565
13.5	1.7335	0.0529

IV. Conclusions

This experiment was successful in obtaining valuable information on the cross section of iridium. Measurements of the (n,2n) cross section were made in 0.25 MeV increments from 8.00 MeV to 9.50 MeV, with the exception of 8.50 MeV, which was excluded due to detector problems. Additional measurements were made in 0.5 MeV increments from 9.5 MeV to 13.5 MeV with the exception of 10.5 MeV where analysis is still ongoing. Overall, this experiment further demonstrated the unique capability of the Tandem accelerator to probe nuclear physics through high precision measurements of the nuclear cross sections. Future study for this experiment would involve re measuring the 8.5 MeV and 10.5 MeV data as well as determining the cross section at 9.75 MeV.

[Bay75] B. P. Bayhurst *et al.*, Phys. Rev. C, **12**, 451 (1975).

[Cha07] M. Chadwick *et al.*, Nucl. Data Sheets, **108**, 2716 (2007).

[END11] *ENDF VIII.0*, 2011, Nuclear Database.

[Goo15] M. Gooden, *GoodFit*, 2015.

[Her84] M. Herman, A. Marcinkowski, and K. Stankiewicz, Nucl. Phys. A, **430**, 69 (1984).

[Kal18] A. Kalamara *et al.*, Phys. Rev. C, **98**, 034607 (2018).

[Kal19] A. Kalamara *et al.*, Eur. Phys. J. A, **55**, 187 (2019).

[Nu224] *Nudat 3.0*, 2024, Nuclear Database.

[Pat07] N. Patronis *et al.*, Phys. Rev. C, **75**, 034607 (2007).

[Qai72] S. M. Qaim, Nucl. Phys. A, **185**, 614 (1972).

[Vla07] R. Vlastou *et al.*, In *Intl. Conf. Nucl. Data Sci. Tech.*, p. 471, 2007.

[Vla17] R. Vlastou *et al.*, EPJ Web Conf., **146**, 11013 (2017).

1.5 High Precision Measurements of the Ratio of the Fission Cross Sections for ^{239}Pu/^{235}U

T. Ordahl, *Saint John's University, Collegeville, MN*; S.W. Finch, *TUNL*

Background HIγS is the highest-flux Compton gamma-ray source in the world. One thing that many researchers want to know for their experiment is the γ-ray flux. The installation of a fission chamber behind the HIγS beam has been proposed to better monitor the flux. The chamber would use ^{238}U and ^{235}U targets to measure the flux.

Purpose We seek to test the uniformity of the distribution of uranium on the targets to ensure that the proposed fission chamber will provide accurate readings.

Methods An alpha-spectrometer was used to measure the average mass as a function of area by covering the targets with aluminum masks of various sizes. This data was then interpreted to find the average radial density of the targets.

Results The results are that the targets are not uniform, having lower densities as radius increases.

Conclusions While the targets do not have uniform density, we can interpolate the mass as a function of radius and adjust for the non-uniformity for use in the proposed fission chamber.

I. Introduction

The High Intensity Gamma-Ray Source Laboratory (HIγS) is currently the highest-flux Compton gamma-ray source in the world. HIγS can produce nearly mono-energetic polarized gamma-ray beams with energies ranging from 2 to 120 MeV with adjustable beam characteristics such as the beam diameter. These features attract researchers from around the world due to these adjustable initial beam conditions. One of the important parameters that is needed by these researchers is the flux of the beam, which currently there is no accurate way to measure leading to either inaccuracies in calculations for the flux or researchers presenting data in a roundabout way to avoid using the flux in the results. As a result, it has been proposed to install a fission chamber at the end of the beam line to accurately measure the flux (θ) . To do this, the cross-section (σ), number of nuclei (n), and time (t) exposed to the γ-ray beam are needed which can be simplified to the equation [Sil24],

$$\text{Counts in Fission Chamber } = n\sigma\theta t.$$

The cross-section and time are known values for an experiment so all that is needed is the number of nuclei. The proposed fission chamber would use thin ^{235}U and ^{238}U targets that had previously been assumed to have a uniform density. The goal of this experiment is to verify and quantify the uniformity of the targets.

II. Methods

To check the uniformity of the targets, a silicon alpha spectrometer was used to measure the number of fission events from the targets, The targets had various aluminum masks placed above them with holes ranging from .25 to 1 in machined through the center (see Fig. 1.16).

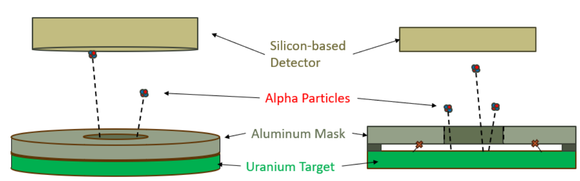

Figure 1.16: Diagram of Target and Mask

The target and mask were placed in the alpha spectrometer which then counted the alpha particles emitted from the area of the target not covered by the mask. Data collection ran until several thousand counts were observed. The ^{235}U was observed for 12 hours for each mask. The ^{238}U was observed for 24 hours for each mask due to less frequent emission of alpha particles. See Figures 1.17 and 1.18 for examples of the spectra. The recorded spectra were analyzed using the software GoodFit. By integrating over the peaks corresponding to the desired isotopes we found the total counts of that isotope.

Following literature [Sil24], we integrated the ^{235}U from 3500-4475 keV and the ^{238}U from 3500-4500 keV. The quantity $counts/(s * cm^2)$ was calculated from the data for each mask and then plotted as a function of mask radius. The data was then fitted to an equation of best fit. The quantity $counts/s$ was converted into micrograms using the half-life of U and plotted as seen in Figures 1.19 and 1.20 [Sil24].

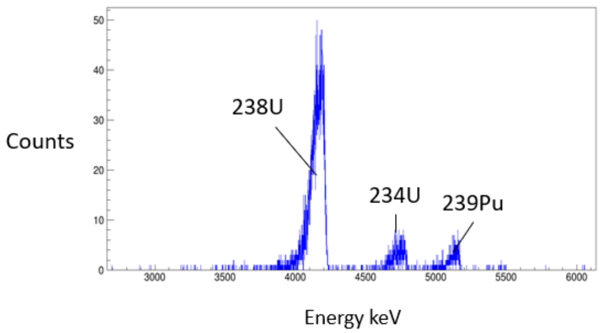

Figure 1.17: Silicon detector spectrum of α particles emitted from ^{238}U

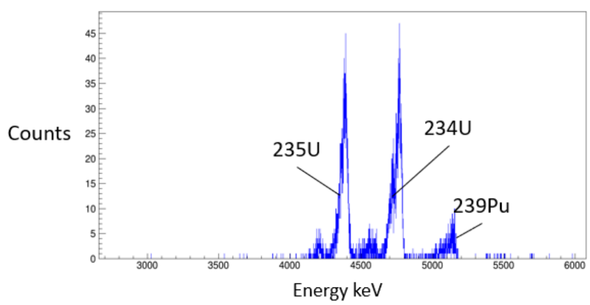

Figure 1.18: Silicon detector spectrum of α particles emitted from ^{235}U

III. Results

As shown in Figures 1.19 and 1.20, for the different mask radii, the targets have an overall decline in average mass as mask radius increases indicating that the targets do not have uniform density. If the targets had uniform density the figures would show a linear horizontal line. However, this does not mean that the targets are unfit for the proposed fission chamber at HIγS, since we can use the fitted equations for any given gamma-ray beam diameter and interpolate the average mass per area to adjust for the non-uniform distribution.

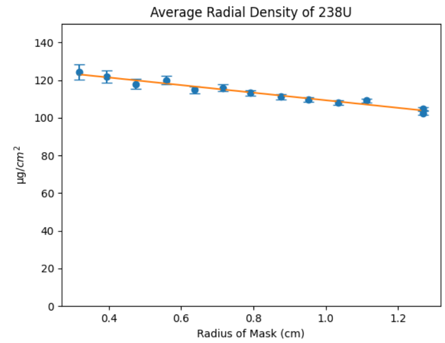

Figure 1.19: Graph Showing Average Radial Density of ^{238}U

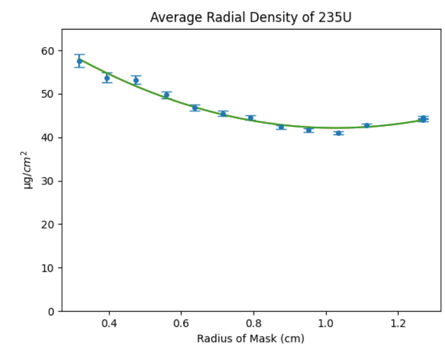

Figure 1.20: Graph Showing Average Radial Density of ^{235}U

IV. Conclusions

This experiment was successful in ascertaining whether the uranium targets had uniform density. We found that the outer areas of the targets had on average a lower density than the center. We propose that the mass per area is interpolated and adjusted for the proposed fission chamber to monitor the flux at HIγS.

[Sil24] J. Silano *et al.*, Nucl. Instrum. Methods, **A1063**, 169234 (2024).

1.6 First Steps Toward a Measurement of $^{12}C(\alpha,\gamma)^{16}O$ at LENA

L. Carroll, *Mount Holyoke College, South Hadley, MA*; C. Marshall, *TUNL*

The reaction rate of $^{12}C(\alpha,\gamma)^{16}O$ dictates the chemical environment from which heavier elements are synthesized during various stages of stellar burning. Despite being a prime determinant of the elemental and isotopic abundances underpinning our universe, the cross section remains incredibly difficult to measure at astrophysical energies. Large uncertainties surrounding this measurement have hindered efforts toward a comprehensive picture of stellar nucleosynthesis. In the Laboratory for Experimental Nuclear Astrophysics (LENA), a time-of-flight method was investigated as a way to combat the obstructive neutron background produced by the $^{13}C(\alpha,n)^{16}O$ reaction. A Bayesian approach to yield curve fitting was also employed for target characterization with the understanding that properties such as thickness, stopping power, and the $^{12}C/^{13}C$ ratio will need to be well-known in a measurement of the desired cross section.

I. Introduction

The $^{12}C(\alpha,\gamma)^{16}O$ reaction is among the most important processes known to take place in stellar environments. A star's lifetime can be broken down into a series of burning stages, each of which proceed via specific synthesis reactions. Near the end of their main sequence lifetimes, stars enter a period of contraction during which hydrogen burning takes place in a shell around the helium core. This process continues until conditions in the core become extreme enough to ignite the existing helium. This ignition marks the start of hydrostatic helium burning, for which ^{12}C and ^{16}O are the primary products. The $^{12}C(\alpha,\gamma)^{16}O$ reaction rate determines the ^{12}C and ^{16}O mass fractions in the universe and is, by extension, responsible for the universal abundances of heavier elements synthesized in subsequent burning stages.

Despite being crucial to early and ongoing nucleosynthesis processes, the $^{12}C(\alpha,\gamma)^{16}O$ reaction rate has not been reliably measured due to its cross section being many orders of magnitude below current detection limits. Even within the limits of what can be experimentally-measured, a large neutron background emitted by the $^{13}C(\alpha,n)^{16}O$ reaction obscures the cross section of interest. The Laboratory for Experimental Nuclear Astrophysics (LENA), located at TUNL, aims to make a precise measurement at energies most likely to constrain the low energy behavior of the cross section. Methods for reducing background and performing necessary target characterizations were explored as first steps toward a measurement of $^{12}C(\alpha,\gamma)^{16}O$.

II. Background Reduction

LENA is equipped with multiple systems intended to aid in the measurement of cross sections at low, astrophysically-relevant energies. Among these is a fast chopper-buncher system capable of producing high-current beam pulses at frequencies up to 4 MHz. Beam pulsing enables additional forms of background suppression, such as a time-of-flight method, making it critical to the measurement of stellar cross sections.

A. Time-of-Flight

Time-of-flight (TOF) measurements will serve as a source of background reduction in this experiment and have been successfully implemented in previous studies of the $^{12}C(\alpha,\gamma)^{16}O$ reaction [Dye74, Mak05]. The purpose of the TOF method is to reliably isolate signals of interest by separating γ-ray and neutron events on a timing spectrum. Beam pulse tests were repeated with CeBr and HPGe detectors to ensure that the electronic setup and data acquisition system in LENA were able to support time-of-flight measurements.

In our electronic setup, a time-to-amplitude converter (TAC) outputs signals derived from the time interval between its start and stop inputs, which are the beam pulse and the detector signal, respectively. An aluminum target was bombarded with a H^+ beam set to pulse at a frequency of 15.625 kHz with an energy of E_p=1004.0 keV, placing on the plateau of the 992 keV resonance in $^{27}Al(p,\gamma)^{28}Si$. After gating around the peak in the resulting TAC spectrum, a coincidence with the detector energy spectrum was found. The condition imposed on our energy spectrum by the timing gate should effectively eliminate background signals. Figure 1.21 compares the raw energy data from the HPGe pulse test to its coincidence spectrum with the gated TAC data. We observe a significant reduction in background, while the characteristic energy peaks for the ^{27}Al(p,γ)^{28}Si reaction are preserved. Repeating this process for the CeBr detector yields less dramatic results, though there is still some visible background reduction.

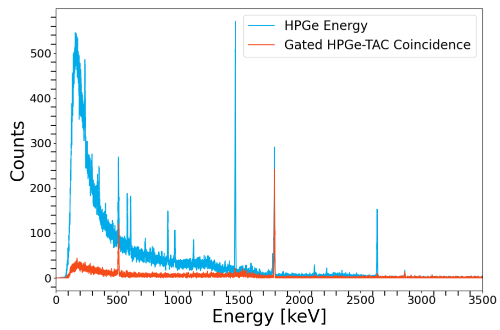

Figure 1.21: The HPGe energy spectrum (blue) and coincidence spectrum (red) between the energy and gated TAC data are shown. There is visible background reduction resulting from the TOF measurement.

Pulse tests performed with the HPGe detector suggested that more dramatic results could be obtained by improving the timing resolution of the detector. Despite yielding some successful elimination of room background, the TAC spectrum from this detector required a gate with a width of approximately 1μs. This result prompted us to work toward improving the detector's timing resolution.

B. HPGe Timing Resolution

To assess the timing resolution of the HPGe detector, a time-to-digital converter (TDC) found the timing difference between the HPGe and CeBr detectors. CeBr is an ideal reference detector for this setup, as its timing resolution is less than a nanosecond. A ^{60}Co source was placed between the detectors, which sat orthogonal to each other. ^{60}Co was chosen for its emission of two coincident γ-rays with known energies of 1173.228 keV and 1332.492 keV [Bé13]. The spectrum of interest in this case is the TDC spectrum for the CeBr set to trigger off of the HPGe. The resulting timing spectrum can be calibrated to give the timing difference between both detectors. Following a baseline run, adjustments were made to the timing filter value for the HPGe, which was initially set at 0.5 μs. The timing filter, itself, is responsible for differentiating and integrating newly-digitized signals. The original TDC spectrum for a timing filter value of 0.5 μs can be seen in Fig. 1.22(a). By gating on full-energy peaks in the ^{60}Co spectrum and bringing the timing filter to 0.25 μs, the resulting TDC spectrum, shown in Fig. 1.22(b), was reduced to an isolated peak with FWHM of 67 channels, corresponding to a resolution of approximately 50 ns.

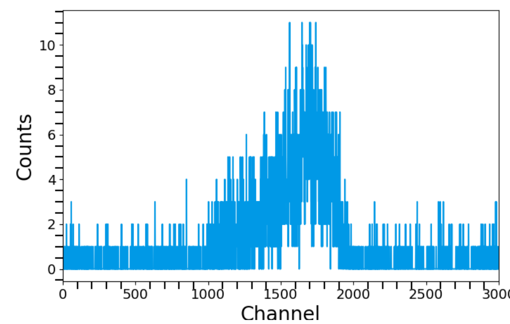

(a)

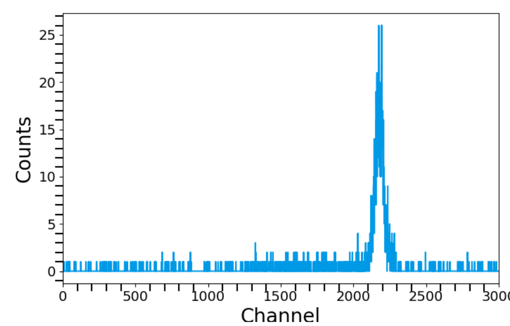

(b)

Figure 1.22: TDC spectra for timing filter values of 0.5 μs (a) and 0.25 μs (b). Figure (b) was obtained by reducing the timing filter and placing gates on full energy peaks in the corresponding energy spectrum.

These changes to the timing resolution of the HPGe detector setup in LENA are expected to help improve background reduction and enable the lab to continue pushing toward lower energies.

III. Target Characterization

A measurement of the ^{12}C$(\alpha,\gamma)^{16}$O cross section will require an enriched ^{12}C target of high isotopic purity. This can be achieved through ion implantation of ^{12}C into a backing that has been properly acid-etched and outgassed to reduce contamination. Before measuring on an implanted target, it was necessary to gather baseline data from natural carbon targets with the goal of extracting information about their properties. Targets were fabricated using two different methods. First, carbon was deposited by exposing tantalum backings to a gas flame in a process called sooting. Flames resulting from incomplete combustion were required to achieve sufficient build-up. The remaining targets were made by floating 40.6 μg carbon foils onto identical tantalum backings. Runs with both the soot and foil targets were carried out at a bombarding energy of 440 keV, allowing us to capture into the tail of the broad 457 keV resonance for ^{12}C(p, γ)^{13}N. For these runs, targets were angled at 45 degrees with respect to the beam, and the HPGe detector was at 90 degrees. Figure 1.23 shows the resulting reaction peak from a carbon foil target, which was believed to possess better surface uniformity than the soot target. The peak, itself, reflects the process of proton energy loss as beam particles experience inelastic collisions with atomic electrons in the target material. Straggling on the low-energy edge results from the slowing down process being highly probabilistic and thus neither immediate nor uniform across all beam particles. The full shape of the resonance peak seen in our carbon target spectrum is a product of both the target profile and the behavior of the ^{12}C(p, γ) cross section as protons span an energy range inside the target. The peak can therefore be used to extract information about certain target properties.

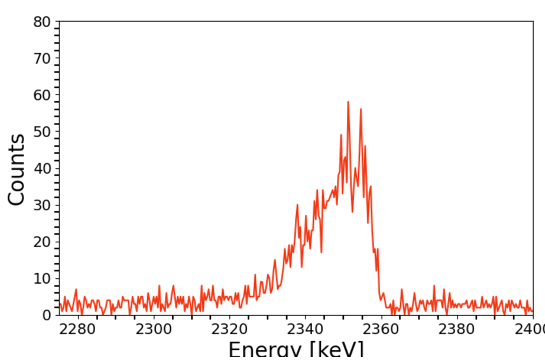

Figure 1.23: Resonance peak from the spectrum collected from a carbon foil target at E$_p$=440 keV.

Target properties we are interested in include physical thickness (dx), incident proton energy loss (dE), stopping power (dE/dx), and the ^{12}C/^{13}C ratio in the target. Proton energy loss is the thickness in energy units, and the stopping power is the rate of energy loss per unit area.

One method investigated for determining target thickness uses a Bayesian statistical approach to fit theoretical yield curves to the spectrum data. Yield is defined as the total number of nuclear reactions per number of incident beam particles and can be plotted as a function of energy. Bayesian statistics allows for active exchange between hypothesis and results, with initial model parameters, known as priors, being set and updated as additional information is obtained about the system. In this case, priors are probability distributions for a set of parameters used to plot a theoretical yield curve. Among these are values such as beam energy, target thickness in energy units, and a straggling constant. Once initial priors have been set, starting values are assigned to each of the yield curve parameters that come as close as possible to the actual value. By setting priors and starting values, a theoretical yield curve can be fit to the resonance peak, as in Fig. 1.24. Once a satisfactory fit is achieved, a Markov chain Monte Carlo simulation is run to produce calculated values for each parameter. In addition to helping determine target thickness, this approach can also be used to obtain the ^{12}C content of a target. Repeating the analysis at a reference resonance for ^{13}C will yield an analogous value, and the ^{12}C/^{13}C ratio can be deduced.

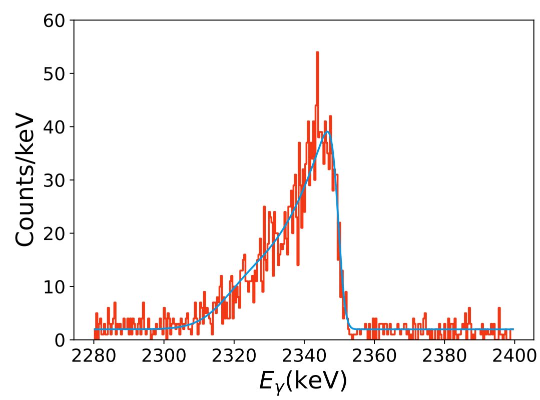

Figure 1.24: Example of a theoretical yield curve fit to the resonance peak in a carbon foil target spectrum.

IV. Conclusions

Beam pulse tests with HPGe and CeBr detectors were used to investigate the utility of TOF measurements in reducing neutron background at low energies. Because background reduction is key to a successful measurement of the $^{12}C(\alpha, \gamma)^{16}O$ cross section, efforts will be made in the future to use enriched ^{12}C targets and to take advantage of active and passive shielding methods in LENA. A Bayesian approach to yield curve fitting was also explored for the purposes of target characterization. Finding ways to reliably extract information about target properties such as thickness, stopping power, and isotopic ratios will be important in the next steps of this experiment.

[Bé13] M.-M. Bé and V. P. Chechev, Nucl. Instrum. Methods, **A728**, 157 (2013).

[Dye74] P. Dyer and C.A. Barnes, Nucl. Phys. A, **233**, 495 (1974).

[Mak05] H. Makii, Nucl. Instrum. Methods, **A547(2–3)**, 411 (2005).

1.7 Evaluating Supernova Sensitivity of Germanium

CELESTE GUERRERO, *University of the Pacific, Stockton, CA*

Background Supernovae release almost 99% of their energy in the form of neutrinos. Being able to detect these neutrinos on Earth would give us valuable information about the life cycle of supernovae.

Methods This project involved simulating the flux of neutrinos that would be detected by an 18 kg germanium-76 detector from a 10 kpc supernova.

Results Our simulation showed that for an 18 kg detector we would expect a total of 0.0012 detected neutrino events from a 10 kpc supernova over a 10 second burst.

I. Introduction

Massive stars reach the end of their life and explode in a supernova process. 99 percent of the energy released from this process is in the form of neutrinos. Neutrinos are small charge-less particles that hardly interact with the matter around them. Therefore, when they reach the Earth, they remain relatively undisturbed from their original state even after their journey. This characteristic allows us to study neutrinos and learn more about stellar process of a supernova explosion and the life cycle of neutron stars.

It is important to establish the usefulness of germanium detector setups for analyzing supernova neutrinos. By measuring the sensitivity of germanium detectors to supernovae, we are able to understand how well detectors in the Ge-mini and LEGEND setups can reveal traits from supernova neutrinos. Using SNOwGLoBeS software, I simulated an 18 kg Ge detector and its measurements of neutrinos from a 10 kpc supernova. This project also helped to refine the code within the SNOwGLoBES simulation software used to make these predictions by making the software useful for charged current interactions on ^{76}Ge nuclei.

II. Methods

I worked with SNOwGLoBES software to simulate the measurements that an 18 kg ^{76}Ge detector would take if a 10 kpc supernova were to go off. I began by creating a channel for the detector. Channels contain the type of neutrino interaction or detection channel that is being simulated. My channel included a ^{76}Ge detector for charged current interactions as we measured electron neutrinos from a supernova. In this channel, I included a detector configuration file to specify the characteristics of the detector such as its size, type, and material. My file specified an 18 kg ^{76}Ge detector. The necessary flux files already existed in the software that I was able to use. The flux contains the distribution of neutrino energies from the supernova simulation; however, as it is integrated over the time of the burst, it is measured as a fluence. The flux that I used measures a ten second neutrino burst. To create cross section files, I constructed data from solar neutrino capture cross sections by ^{76}Ge into a GLOBES format that the software would understand. The smearing files specify the energy resolution of the detector and how it affects the neutrino spectra. These smearing files are then used to construct a matrix that represents how true neutrino energies are smeared into detected energies. I used the formula

$$\sigma = \sqrt{a^2 + b^2 E + c^2 E^2} \tag{1.1}$$

to define the Gaussian detector resolution where $a = 0.068$, $b = 0.02$, and $c = 0.001$ with E in keV. The channel inputs would allow the simulation software to output the interaction rates in ^{76}Ge.

III. Results

Figure 1.25 shows a GVKM flux which is measured as a fluence as it is integrated over a 10 second burst. The graph displays the count in neutrinos per second for each neutrino flavor. The cross sections are displayed in Fig. 1.26 in log scale.

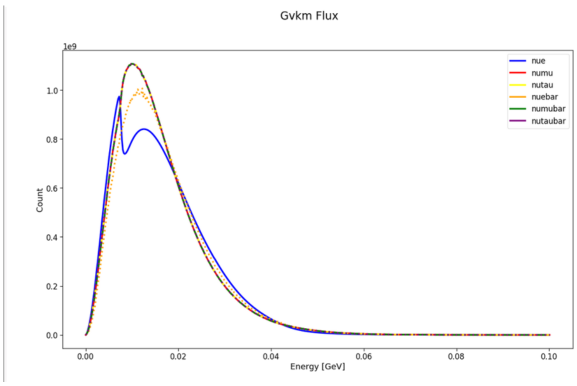

Figure 1.25: GVKM Flux

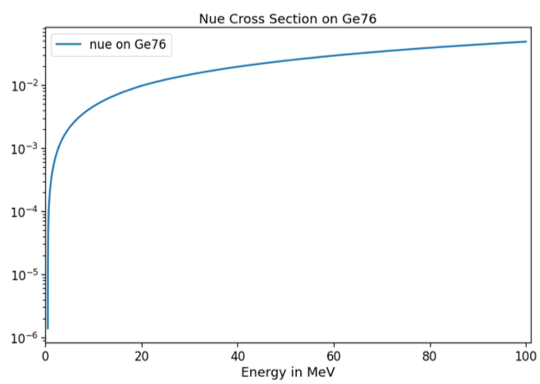

Figure 1.26: Solar neutrino capture cross section on ^{76}Ge

Figure 1.27 shows that there are low interaction rates for the smeared detection rates. The electron scattering is only a fraction of the electron neutrino interactions. This is is similar to the unsmeared interaction rates shown in Fig. 1.28. The two figures display similar distribution and shape as well as proportion between the electron neutrino and electron scattering interactions.

Figure 1.29 shows a table of the interaction rates for the 18 kg detector simulated by the SNOwGLoBES software. I then was able to scale the ^{76}Ge detector to the 200 kg currently employed by LEGEND to make predictions for the interaction rates that would occur for the 10 second burst if a 10 kpc supernova were to go off. Ge-mini uses natural germanium, therefore, I had to scale by the fraction of the ^{76}Ge isotope to get the event numbers.

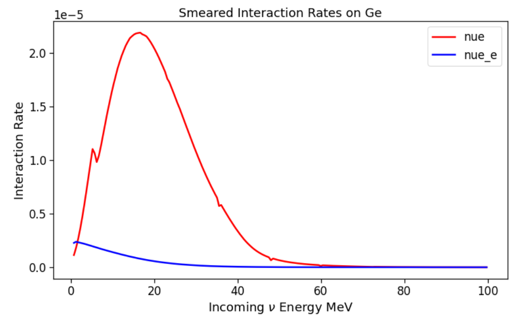

Figure 1.27: Smeared Interaction Rates on Ge for nue and nue$_e$

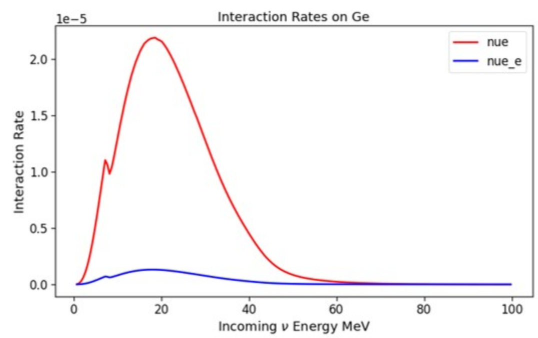

Figure 1.28: Interaction Rates on Ge for nue and nue$_e$

Detector:	18kg Dect	LEGEND	Ge-mini
Nue_e:	6.549e-05	7.277e-04	5.076e-06
Nue_Ge76:	0.00108	0.012	8.371e-05
Total ES:	6.549e-05	7.277e-04	5.076e-06
Total Events:	0.0012	0.0127	8.8778e-05

Figure 1.29: Table of interaction rates for individual detectors within the 10 second burst

IV. Conclusions

The small event values may be a result of the detector size and the short time of a 10 second burst. The total neutrino events for the 18 kg detector is 0.0012. Total LEGEND events are 0.0127 and Ge-mini events are 8.8778e-05. We used ^{76}Ge due to access to data from solar neutrino capture cross sections. Future steps include analyzing other isotopes of germanium and their measurements of neutrino events.

1.8 GNN Improves the tracking of Pions in CLAS12

K. Mencke, *Lawrence University, Appleton, WI*

Background Machine learning techniques, and graphical neural networks (GNN) in particular, have been used extensively for data analysis in high energy physics; however, its uses in nuclear physics have not been as widely explored. We report on the use of a GNN to enhance tracking of π^- in CLAS12 experiments at Jefferson Lab (JLab). Pion tracking is important because of their use in detecting Λ which decay weakly into a proton-pion pair.

Purpose Current reconstruction of pion tracks is poor and is unable to be used for lambda measurements. Our goal was to use a GNN to improve pion z vertex reconstruction, and improve resolution of Λ invariant mass.

Methods We used machine learning to improve pion tracking. Specifically we used the Python library PyTorch. Our training dataset was made from detector data and was trained against Monte Carlo simulations. Both the JLab and the Duke computing clusters were used.

Results The GNN produced an average error from truth of 1.1 cm compared to 3.3 cm for the reconstructed data (rec). It also had a better standard deviation of the error of 3.3 compared to 11.6 for the rec. Cuts were made based off this prediction which saw a improvement in seeing the lambda peak in invariant mass spectra.

Conclusions The GNN performed well compared to the rec in getting the pion z vertex. Promise was also shown in using this prediction to make cuts to improve the invariant mass peak resolution. More work still needs to be done though on using this prediction to make cuts. Improvements could be made in size of the dataset and length of training.

I. Introduction

Pions are of interest because lambda (Λ) particles decay weakly into proton and pion pair, $\Lambda \rightarrow p\pi^-$. Because of the weak decay, the polarization of the lambda is preserved in the cross section of the proton and pion, which make lambdas an attractive candidate to look at spin dependent Parton Distribution Functions (PDF's). In addition, the weak decay also causes the lambda to travel further down the beam line (z direction) before decaying. Looking at the invariant mass of the proton pion pair, one should be able to see the lambda peak at 1.12 GeV. In the CLAS12 experiment, seeing this peak is difficult because of the large background from non-strange final states. The CLAS12 experiment contains a six-coil torus magnet and a high-field solenoid magnet [Bur20]. Measurements are made in the drift chambers which determine particle trajectories [Mes20]. This also allows for the identification of particles' momentum [Mes20].

We seek to use a graphical neural net (GNN) to improve the tracking of pion z vertex and to improve the resolution of the lambda peak in the invariant mass of pion proton pairs. GNN's are a generalization of convolution neural networks (CNN) with the benefit of being able to handle a variable input size [McE23]. One of the inputs to our GNN is hits in a detector, which is variable, so this was a main factor in the choice of a GNN. Data from the CLAS12 experiment was used as input to the GNN, while the truth was from Monte-Carlo simulations also from Jlab.

II. Methods

All of the data input to the GNN was obtained from Jlab CLAS12 experiments. The data from Jlab used in the GNN was formatted into graphs using the *torch_geometric* python library. The x part of the data (the inputs) was made up of several parts. The first was detection hits and direction of hit obtained from the drift chambers in CLAS12. The second was momentum of particle. The third was reconstruction's guess at the vertex modified with a random distribution around this guess at the vertex. All of these parts were done for proton and pion pairs. The proton and pion tracks were also linked by edges. The y part of the data was the z part of pion vertex from Monte-Carlo simulations. A standard ratio of $80\%, 10\%, 10\%$ was used for training, validation, and testing. This means that 80% of the data is used to train the GNN, 10% is used for validation, and 10% is used for evaluation. For some runs, the GNN was trained on the whole dataset, and then a separate dataset was improved for testing. Once created, the data was transported over to the Duke Computing Cluster (DCC), which was where the GNN was trained.

The python library *torch_geomtetric* contained most of the functions used to make the neural net. The GNN contained 3 hidden layers and relu was the activation. Relu is a common activation function (activation functions are used to introduce non-linearity to neural nets) that is defined as $y = x, x \geq 0$ and $y = 0, x < 0$. Dropout layers were used to counter over training. Root mean squared error (rmse) between the predicted pion z vertex and the true z vertex was used as the loss function. The biggest run was for 50 epoch with a 35000 event dataset. Generally a 5 epoch run was enough to see good results, and after 40 the improvements were small. Slurm on the DCC was used to evaluate and train most of the GNN's. Analysis of how the GNN performed was mainly a comparison with the current algorithms (rec) guess at the z vertex. This was done by taking the difference between prediction and truth event by event for both the GNN prediction and the rec prediction.

III. Results

The first result is the improvement of prediction of z component of pion vertex compared to the current reconstruction (rec) using a GNN. A GNN was trained on a dataset of 40000 events for 40 epochs. A histogram of the distribution of pion vertex's is displayed in Fig. 1.30. The mean absolute difference between the predicted and the truth was 1.1 cm. The mean absolute difference between the reconstructed and the truth was 3.3 cm. In addition, a Gaussian was fit to the distribution of each of these errors. From this Gaussian, a standard deviation of 3.3 was determined for the predicted compared to a standard deviation of 11.6 for the reconstructed. Overall, the GNN showed a marked improvement over the reconstructed compared to the current rec.

Improving the prediction of pion vertex is good, but what really matters is how pions relate to lambdas. To start with, we subtracted off the initial scattered electron, so that we get how far down the beam line the pion vertex is. Lambdas decays take a while, so we expect pion that come from lambdas to be further down the beam line than ones that do not come from lambdas. If we then make cuts on the pion vertex (minus the scattered electron), and only accept events where the vertex is down the beam line, the resolution of the lambda peak should be improved. In Fig. 1.31, we show the results of doing this. This was previously impossible to do with the reconstructed vertex. Making cuts of both 1 cm and 2 cm showed an improvement in the lambda peak, when compared to raw invariant mass spectra. However, the statistics (number of counts) for both cuts, went down. In the 1cm case it suffered about a 50% reduction in number of counts, while in the 2 cm case there was around a 80% reduction in the number of counts.

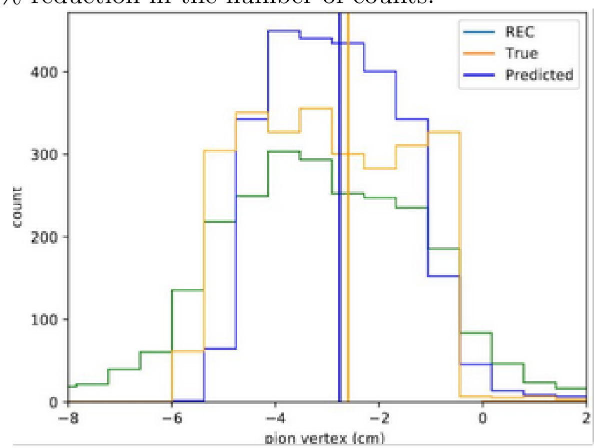

Figure 1.30: Distribution of pion vertices. Orange is the true value obtained from Monte-Carlo simulations. Blue is what the GNN predicts for the pion vertex. Green is the current reconstructed prediction for pion vertex. The orange and blue vertical lines, are the mean of the distribution of truth and predicted respectively.

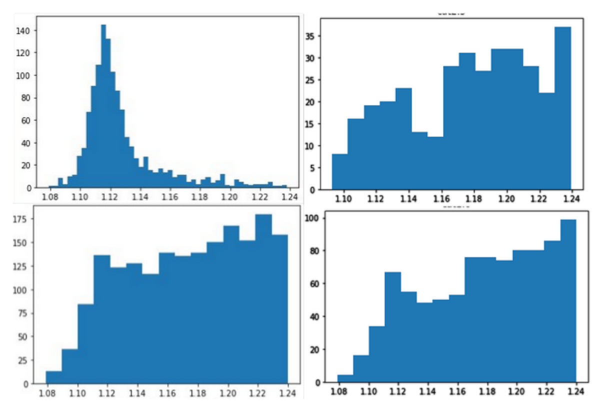

Figure 1.31: Invariant Mass of lambdas. All of the x-axes are in units of GeV. Y-axis is in units of number of counts. Top left is only lambda particles (ideally what we would get). Bottom left is what an invariant mass of experimental data look like. Top right, is a cut on the pion vertex of 2.5cm. Bottom right is a cut on the pion vertex of 1.0 cm.

IV. Conclusions

Our goal was to make a GNN to improve the tracking of pions in Jlab's CLAS12 experiment. Improving the tracking of these pions can help the study of lambda's and spin-dependent pdf's. We showed a marked improvements in the prediction of pion z vertex, when compared against the current reconstructed and trained against Monte-Carlo simulations. Improvements can still be made though. A 1 cm error is a factor of 3 improvement, but it is still a high amount of error. In addition to improving the prediction of pion z vertex, we also showed how this could be used to improve the reading of lambda's. We showed qualitatively in Fig. 1.31, an improvement in the resolution of the lambda peak at 1.12 GeV. More work still needs to be done on this. A quantitative improvement must be shown, by using fitting algorithms and to demonstrate the improvement of making cuts on the pion vertex. Improving the statistics (getting more counts) is also necessary to make it a useful result. We believe this can be done, by simply using more data. An improvement in theoretical calculation would be the final result we could add.

[Bur20] V. Burkert *et al.*, Nucl. Instrum. Methods, **A959**, 163419 (2020).

[McE23] M. McEneaney and A. Vossen, J. Instrum., **18**, P06002 (2023).

[Mes20] M. Mestayer *et al.*, Nucl. Instrum. Methods, **A959**, 163518 (2020).

1.9 Development of Affinity through EIC Kinematics

P. Smith, *Lebanon Valley College, Annville, PA*; A. Vossen, *Duke University, Durham, NC*

Background With the future Electron Ion Collider (EIC) bringing a new set of collision experiments covering a much larger kinematic region than ever before, it is important to understand which regions in this kinematic space are associated with specific theoretical factorization theorems. Making these connections allows us to more effectively utilize EIC data to understand the internal structure of nucleons.

Purpose Further develop the "affinity tool," which gives a quantitative and visual representation of the viability of a given factorization method in a kinematic bin.

Methods Results from Monte-Carlo simulations utilizing Pythia were used to calculate momenta-based ratios necessary for calculation of affinity. These results were compared with other results using Gaussian distributions for quark kinematics.

Results The current calculation method of affinity was refined to an agreement between both the Monte-Carlo method and the Gaussian distribution method.

Conclusions Use of Monte-Carlo simulations can provide a detailed analysis of the viability of factorization theorems for kinematics for EIC experiments.

I. Introduction

The complex internal structure of hadrons is a topic which requires precise understanding of Quantum Chromodynamics (QCD) factorization theorems. These theorems allow for a partonic description of hadrons through the results of inclusive and semi-inclusive deep-inelastic scattering (SIDIS) experiments. However, not every factorization theorem can be applied at every point in kinematic phase space, as corrections can grow large. Consider transverse momentum dependent (TMD) factorization [Bog22], which separates these processes into nonperturbative TMD parton distribution functions (PDFs) and fragmentation functions (FFs) as well as a perturbative hard scattering cross section [Kot95, Mul96, Bog22, Boe98]. Here, it is imperative that the momentum of the struck quark is independent with the momenta of partons which are spectators to the hard collision [Bog22]. Without this, and various other assumptions, TMD factorization is not applicable.

In this project, we aim to map the viability of TMD factorization over the region of kinematic phase space that will be reached by the Electron Ion Collider (EIC). The tool, called "affinity", has been developed by Boglione *et al.* via 'indicator ratios' calculated from the partonic kinematics of a SIDIS event [Bog22, Ans11]. Since these kinematics cannot be extracted from data, methods for estimation must be tested. We employ Pythia-based Monte-Carlo simulations for our data.

II. Methods

Now we outline the method of mapping the *current* region, where TMD factorization is valid. This method uses various indicator ratios that quantify the assumptions made in the proof of TMD theory. The first of these is called the *general hardness* ratio,

$$R_0 \equiv \max\left(\left|\frac{k_i^2}{Q^2}\right|, \left|\frac{k_f^2}{Q^2}\right|, \left|\frac{\delta k_T^2}{Q^2}\right|\right).$$

The smallness of this ratio, $R_0 \ll 1$, is necessary for a partonic description of the SIDIS process. This is because the mass scale of k_i and k_f must be small relative to the momentum transfer, Q^2 [Ans11].

The next ratio separates the current region from two other regions called *target* and *central.* Further explanation of these regions can be found in Boglione *et al.* [Ans11]. The *collinearity* ratio is defined by

$$R_1 \equiv \frac{P_h \cdot k_f}{P_h \cdot k_i}.$$

This ratio indicates the outgoing hadron is produced from the final quark, as opposed to the initial quark by checking which it is more collinear with. Thus, the ratio must be small for the current region as we assume the hadron is produced from the final quark.

The final ratio that will be considered in this paper is the *transverse hardness* ratio. This ratio is useful for indicating $2 \to 1$ kinematics, which dominates the TMD regime [Bog22]. It is defined as,

$$R_2 \equiv \frac{|k^2|}{Q^2},$$

where $k \equiv k_f - q$ [Bog22]. As with the other two, we require R_2 to be small to be in the current region.

With these ratios defined, we may then set a threshold for their values. We use 0.3 for future calculations. We define affinity for a given kinematic bin as the proportion of the events within that bin in which all three ratios are less than the given threshold value.

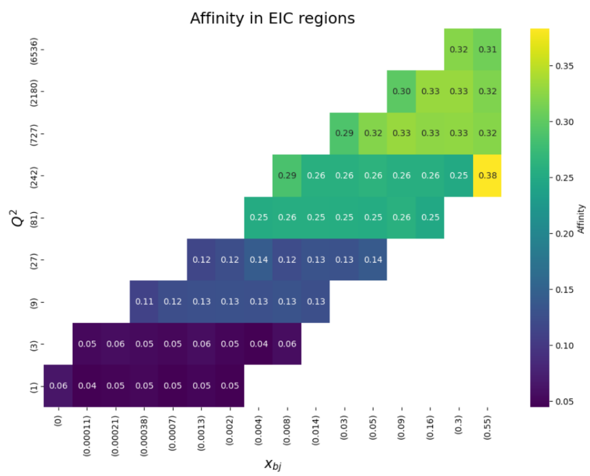

Figure 1.32: Affinity for EIC kinematics binned by x_{Bj} and Q^2.

III. Results

Next we present the current analysis of affinity across the EIC kinematic reach. First, consider Figure 1.32, which contains our affinity values binned by x_{Bj} and momentum transfer Q^2. We see that the affinity values rise with Q^2, but stay relatively constant across x_{Bj}. Both of which are expected.

We also present affinity plotted by x_{Bj} and Q^2 values separately in Figures 1.33 and 1.34. Each point contains 10% of the total events and is plotted at the average of that bin.

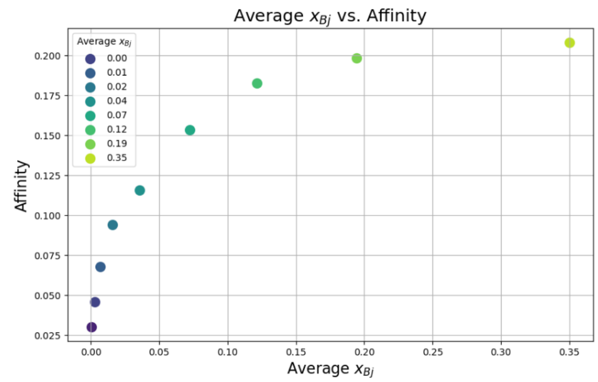

Figure 1.33: Affinity binned by x_{Bj}.

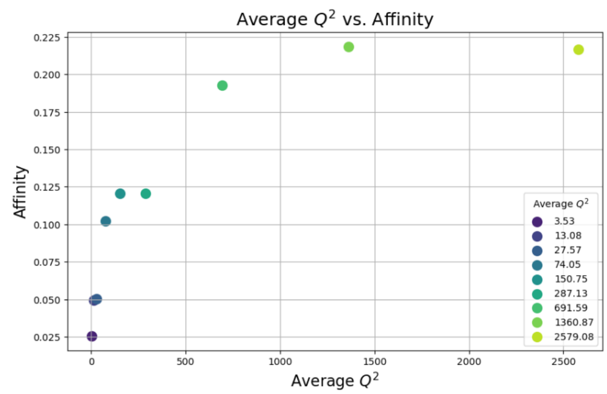

Figure 1.34: Affinity binned by Q^2.

IV. Conclusions

Overall, the patterns found in the affinity calculations match those predicted by TMD theory. It should be noted that further kinematic binning is necessary for a better mapping of the current region. Further, the current trends provide motivation to utilize the framework for the target and central regions as well.

We propose further investigation into affinity over the range of kinematic variables: $y_h, q_T/Q$, and P_h^T for future investigation. We also wish to compare these binnings to the results of the target and central region calculations in order to create a full mapping of affinity over the entirety of EIC kinematic phase space.

[Ans11] M. Anselmino, V. Barone, and A. Kotzinian, Phys. Lett. B, **699**, 108 (2011).

[Boe98] D. Boer and P. J. Mulders, Phys. Rev. D, **57**, 5780 (1998).

[Bog22] M. Boglione *et al.*, J. High Energy Phys., **04**, 084 (2022).

[Kot95] A. Kotzinian, Nucl. Phys. B, **441**, 234 (1995).

[Mul96] P. J. Mulders and R. D. Tangerman, Nucl. Phys. B, **461**, 197 (1996), [Erratum: Nucl.Phys.B 484, 538–540 (1997)].

Research Based at CERN

Chapter 2

2.1 Probing Quantum Interference and Spin Effects in Parton Showers through Multi-Point Energy-Energy Correlators

M. Gratrix, *University of Connecticut, Storrs, CT*; A.T. Arce, *Duke University, Durham, NC*

Background When high-energy collisions occur at the LHC, energetic partons like quarks and gluons manifest as jets. This production process is initiated with a parton shower, which obscures critical information about the original quarks and gluons.

Purpose This project develops an ATLAS measurement of multi-point energy-energy correlators (EECs) observables. This directly allows quantum aspects to be probed in the jet substructure, focusing on spin interference effects.

Methods This project explored multi-point EECs using artificially generated data to identify quantum interference patterns arising from parton spin dynamics in the angular distribution of energy.

Results Gluon-initiated jets consistently displayed greater energy density than quark-initiated jets, aligning with theoretical predictions. However, our observations showed a phase shift of $\pi/2$ from the theoretically predicted pattern.

Conclusions Observed interference patterns using Monte Carlo generators revealed discrepancies with theoretical predictions. The reason for the potential inconsistencies between the generators and theoretical descriptions have yet to be determined and will be the subject of additional exploration.

I. Introduction

The ATLAS experiment at the LHC has significantly extended our understanding of jet substructure by providing detailed measurements of particle jets formed in high-energy proton-proton (pp) collisions. Jets arise as partons (quarks and gluons) undergo a shower, emitting further partons before hadronizing. This QCD-governed process complicates the identification of the original partons due to the intricate nature of hadronization [Pes95]. Understanding jet substructure is crucial for probing QCD's fundamental aspects and identifying signatures of new physics beyond the Standard Model [Sch18].

Recent theoretical work has indicated the capability of multi-point energy-energy correlators (EECs) to observe the quantum aspects of parton interactions [Che21]. EECs capture spin interference effects, providing detailed angular correlations between energy deposits in jets. These correlators significantly enhance jet substructure analysis with their unique ability to distinguish between quark-initiated and gluon-initiated jets.

Incorporating spin correlations in event generators has advanced our ability to investigate parton showers, capturing spin dynamics and helicity correlations [Her19]. This capability is essential for validating new jet substructure analysis methods, providing a concrete foundation for our research.

This study develops and validates a method for measuring multi-point EECs using generated data. By focusing on quantum interference patterns, we aim to refine jet substructure analysis and provide deeper insights into parton dynamics and fundamental forces, ultimately enhancing our understanding of QCD and high-energy particle behavior.

II. Methods

Dijet events occurring when two jets are formed due to a pp collision were generated using the Herwig event generator with a center-of-mass energy (Q) of 1 TeV. Herwig was chosen for its robust implementation of an angular-ordered parton shower, which can model QCD effects [Her19]. We focused on the processes $gg \to gg$ and $gg \to q\bar{q}$ to investigate quantum interference effects between spinning gluons.

Jet reconstruction with the anti-k_t algorithm and radius parameter of 0.5 successfully identified jets from the generated data. Initially, the FastJet package in Python was utilized for this task [Cac12]. Subsequently, the transition was made to the Julia JetReconstruction package due to its advantages in numerical computations. This transition involved collaboration with the package creator to update and refine the package, ensuring it met the specific requirements of the analysis [Ste24]. The Julia implementation provided faster and more efficient calculations, which is crucial for handling large datasets.

An analysis of jets' transverse momentum (p_T) distribution post-reconstruction showed a noticeable peak at low p_T values, identified as noise. Additionally, a second peak starting around 900 GeV indicated high-energy jets. A p_T cut-off of 900 GeV was implemented to isolate these high-energy dijet events.

After calculating the angular separation, ΔR, between all triplets of particles $(\hat{n}_1, \hat{n}_2, \hat{n}_3)$ within a jet, sets were filtered based on the largest angular separation (θ_L) falling within the 0.16-0.32 range. This enabled a focus on the squeezed limit as displayed in Figure 2.1, which is necessary for observing spin interference effects [Che21].

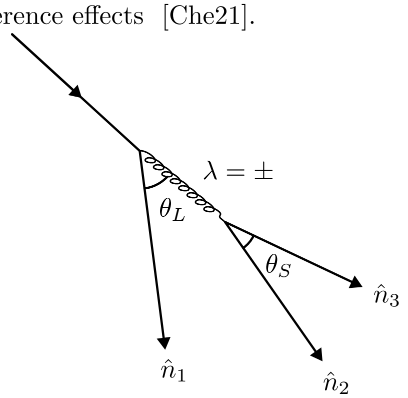

Figure 2.1: Schematic representation of the angular configuration in a parton shower, illustrating the largest angle (θ_L) and the smallest angle (θ_S) among three emitted particles $\hat{n}_1, \hat{n}_2, \hat{n}_3$. This setup highlights the squeezed limit where $\theta_S \ll \theta_L$, relevant for observing quantum interference effects between the gluon helicity states $\lambda = \pm$.

The analysis utilized Julia for its superior performance in handling intricate numerical computations. It focused on computing multi-point EECs to detect quantum interference patterns resulting from parton spin dynamics. As discussed earlier, the analysis centered on jets and constituent data. The process for these calculations is described below.

The angular separation between jet constituent particles was calculated using the LorentzVectorHEP package [Lin22]. As described earlier,triplets of particles were selected, and EEC(3) values and corresponding weights were calculated based on the $(\theta_L\theta_S)^2$ factor:

$$w = \frac{(\theta_L\theta_S)^2 \cdot p_{T1} \cdot p_{T2} \cdot p_{T3}}{(\sum p_T)^3}. \tag{2.1}$$

Angles θ_L and θ_S came from the triplet's sorted ΔR values. The transverse momenta, p_{Tn}, for each particle $n = \{1, 2, 3\}$ is dotted with the square of the angles, normalized by the cubed sum of constituent transverse momenta in the jet, p_T.

The angle ϕ between the planes formed by the triplet of particles was computed to identify spin interference patterns, as illustrated in Figure 2.2. This angle helps illustrate the correlation between the emitted particles and the gluon's spin state.

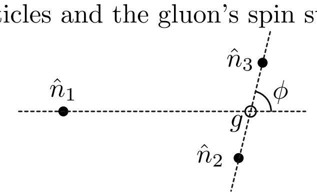

Figure 2.2: Another angle of the angular configuration in the squeezed limit shown in Figure 2.1 from the detector perspective looking *down* a jet. The angle ϕ is defined between the planes formed by the $\hat{n}_1$ and gluon (g) emission and the particles $\hat{n}_1$ and $\hat{n}_2$, illustrating the correlation between the emitted particle energies and the gluon's spin state.

In the three-point energy correlator study, the squeezed limit configuration should reveal quantum interference patterns between the helicity states of intermediate gluons. This phenomenon resembles a double-slit experiment in spin space, with the helicity states ($\lambda = \pm$) of virtual gluons replacing the slits. The interference terms in $|A_+(\phi) + A_-(\phi)|^2$ exhibit a $\cos(2\phi)$ pattern [Che21]. This pattern, modulated by the angular separation θ_S, directly reflects the quantum interference of gluon spin states and emphasizes the non-trivial spin structure of QCD.

Recent theoretical analyses indicate that the three-point correlator in the squeezed limit is sensitive to these spin interference effects [Che21]. This offers a new observable for studying transverse spin dynamics in high-energy jets. This study utilizes this property to analyze the energy density's angular dependence, particularly anticipating the energy density to exhibit a $\cos(2\phi)$ dependence.

III. Results

We made an intriguing discovery after performing the dijet event generation and EEC(3) calculation for 10,000 events and focusing on the particle scale. The energy distribution showed a notable phase shift of $\pi/2$ from theory [Che21]. The resulting interference pattern from virtual gluon spin states showed a high energy density at $\phi = 0$, π, and 2π, as visually presented in Figure 2.3. This phase shift indicates our generated collisions aren't in agreement with theoretical descriptions. The cause of this discrepancy remains unknown, necessitating further investigation.

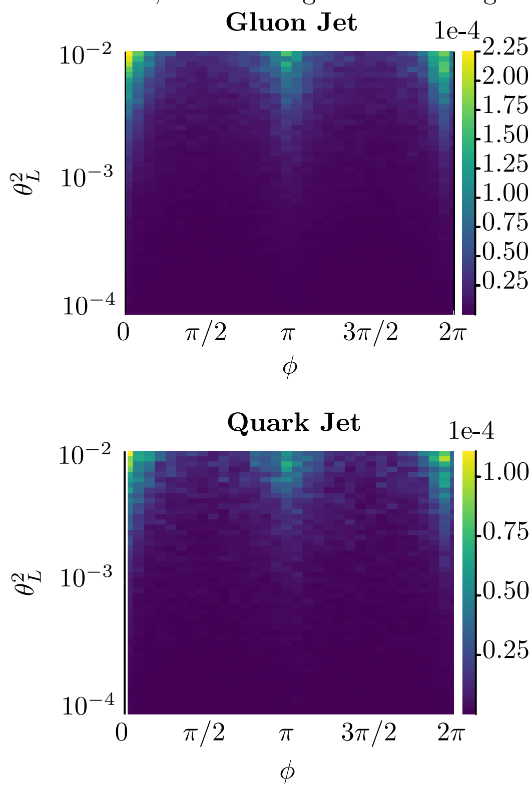

Figure 2.3: Energy distributions for gluon-initiated (top) and quark-initiated (bottom) jets as a function of the angle ϕ and the squared angle θ_L^2. The gluon jet exhibits a stronger energy density, which is evident from the higher intensity regions, which aligns with theoretical predictions. Both distributions show interference patterns, but the observed phase shift does not match the theoretical expectations, indicating complex dynamics in parton interactions.

The findings in Figure 2.3 indicate that jets triggered by gluons exhibit higher energy densities than those initiated by quarks. This heightened energy density in gluon jets implies greater particle multiplicities when compared to quark jets. Studies showing a higher average particle multiplicity in gluon jets corroborate these findings, displaying more substantial energy densities [Gal13].

The interference patterns alone do not distinguish between gluon and quark-initiated jets as anticipated [Che21]. However, the range of energy densities still serves as a crucial identifier. Gluon jets have a higher range of energy densities, enabling the identification of the initial parton based on the distribution range. This indicates that while the interference patterns provide insights, the energy density range remains a powerful tool for distinguishing between different jet types.

IV. Conclusions

Our findings show that gluon and quark-initiated jets have different energy density ranges. The energy density range can help us determine the initial parton type, showing value in EECs for distinguishing what partons initiate a jet. Despite these initial similarities, there are concerning differences in the phase shift between gluon and quark jets compared to theoretical predictions. Discrepancies between our results and theory suggest room for further investigation into different event-generation techniques. The cause of these deviations could be due to limitations in the Monte Carlo simulations or numerical calculation errors. Overall, this study contributes to expanding our knowledge in this specialized subfield of jet substructure and its proximity to QCD as a whole.

[Cac12] M. Cacciari, G. P. Salam, and G. Soyez, Eur. Phys. J. C, **72**, 1896 (2012).

[Che21] H. Chen, I. Moult, and H. X. Zhu, Phys. Rev. Lett., **126**, 112003 (2021).

[Gal13] J. Gallicchio and M. D. Schwartz, JHEP, **2013** (2013).

[Her19] Herwig Collaboration, *Angular-ordered Shower: Spin and Soft Correlations*, `https://herwig.hepforge.org/tutorials/showers/qtilde.html?highlight=spincorrelations#spin-and-soft-correlations`, 2019, Accessed: 2024-07-22.

[Lin22] J. Ling and contributors, *LorentzVectorHEP.jl*, `https://github.com/JuliaHEP/LorentzVectorHEP.jl`, 2022, MIT License, Copyright (c) 2022 Jerry Ling proton@jling.dev and contributors.

[Pes95] M. E. Peskin and D. V. Schroeder, *An Introduction to Quantum Field Theory*, Westview Press, 1st edition, 1995.

[Sch18] S. Schramm and ATLAS and CMS Collaborations, In *Proceedings of the 2018 Large Hadron Collider Physics Conference*, 2018, ATL-PHYS-PROC-2018-163.

[Ste24] G. A. Stewart *et al.*, *JetReconstruction.jl*, `https://github.com/JuliaHEP/JetReconstruction.jl`, 2024.

2.2 Background Effects from Measuring Entanglement in Top Quark Decays

K. Vandra, *Villanova University, Villanova, PA*; A.T. Arce, *Duke University, Durham, NC*

Background: This project aims to aid in the measurement of entanglement between orbital and spin angular momenta in top quark decays, an area largely unexplored beyond photon systems. Particularly, this project will focus on the single top decay mechanism, $t \to W^+ b$.

Purpose: The motivations for this project lie in deepening our understanding of how background processes contaminate findings at the LHC, advancing both theoretical frameworks and experimental techniques in the study of particle interactions.

Methods: Using MadGraph5, we simulated 10,000 proton-proton collision events to study top quark decay, analyzing the resultant bottom quark and W^+ boson, which decays into a lepton and neutrino. The data, transformed into the correct reference frame, was used to extract angles for constructing a density matrix to determine entanglement, with additional background events generated to assess contamination.

Results: The results of this project are that we have effectively designed a framework to significantly eliminate background contamination from our analyses. This background would greatly alter our potential entanglement measurements.

Conclusions: Future work concerning extracting the necessary reduced amplitudes will be conducted.

I. Introduction

This research centers on the analysis of single top quark decay, a process initiated by the collision of two protons that results in the production of a top quark and a W boson. The W boson subsequently undergoes leptonic decay, producing a lepton and a neutrino. Figure 2.4 shows a Feynman diagram for the process. Our goal is to extract reduced amplitudes by analyzing the helicity fractions associated with this decay. A significant challenge in this analysis is differentiating the true signal from background processes that can resemble the decay of interest. By applying specific filtering techniques, we aim to isolate the genuine decay events, thereby improving the accuracy of our measurements.

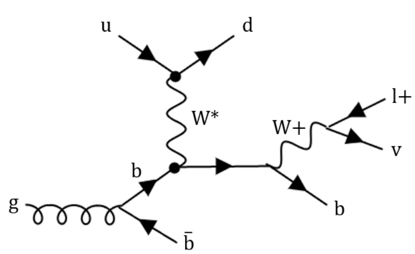

Figure 2.4: Feynman diagram showing the type of the collision and process of interest.

II. Methods

As detailed in the study by J.A.A Saguliar [AS24], a specific angle, denoted as θ^*, is required to determine the reduced amplitudes. Extracting this angle necessitates transforming all events into a unified reference frame due to rotational symmetry. Since each event can occur in any orientation within the detector, it is essential to standardize the orientation for analysis. The procedure involves a series of rotations and boosts. Initially, each particle is boosted into the rest frame of the top quark. Subsequently, the z-axis of the current coordinate system is aligned with the momentum of the top quark. Following this, a second rotation aligns this new z'-axis with the momentum of the W boson. These rotations are Euler rotations, which involve three consecutive rotations about the axes of the coordinate system. Specifically, an Euler rotation typically includes a rotation about the z-axis, followed by a rotation about the y-axis, and finally another rotation about the z-axis. This allows for the transformation of the coordinate system to any desired orientation. Finally, all particles are boosted into the W boson rest frame. This transformation allows us to examine the angles between the decay products of the W boson, ultimately determining the θ^* angle.

After obtaining the θ^* angles for each event, we proceed by fitting our data to the probability density function shown below, achieved by plotting the cosine of these angles:

$$\frac{1}{\Gamma}\frac{d\Gamma}{d\cos\theta^*} = \frac{3}{8}F_+(1+\cos\theta^*)^2 + \frac{3}{4}F_0\sin^2\theta^* + \frac{3}{8}F_-(1-\cos\theta^*)^2. \tag{2.2}$$

This function serves as our fit model for data that consists solely of the signal. With the signal analysis completed, we turn our attention to background processes. In this context, "background" refers to any processes occurring in the detector that might be mistaken for the process of interest, which, in this case, is the decay of a single top quark. Although numerous background processes can occur, the three most significant ones are W boson production with associated jets, Drell-Yan processes, and top-antitop quark pair production.

To address these background processes, we utilized MadGraph5 and a custom script to generate a file containing both signal and background events, weighted proportionally to what the detector would realistically observe. Subsequently, we developed a script aimed at filtering out only the single top events. This filtering process involved several steps. First, quarks and leptons were selected based on cuts applied to their pseudorapidity and transverse momentum. Next, random numbers between 0 and 1 were used to relabel jets according to their tagging efficiency, with the bottom quark having a tagging efficiency of approximately 0.7 and the light quarks a tagging efficiency of about 0.1. Finally, events that did not meet the desired final state particle count were excluded. The remaining events consisted of one lepton, one tagged jet, and one untagged jet.

In the final step, a neutrino was reconstructed for each event. Neutrinos are treated as "missing transverse momentum". The process begins by calculating the vector sum of the momenta of all particles in the event, which is then projected perpendicular to the beamline. If this vector sum in the transverse plane is zero, the negative of the x and y components of the summed momenta represents the momentum of the neutrino in that event.

With the events now filtered, we have a more refined sample to apply the fit to. Although this results in a smaller number of events, applying the fit to the probability density function (PDF) with this filtered sample yields a distribution that more closely resembles that of the signal alone. From this refined fit, we can further extract the helicity fractions, which are crucial for determining the reduced amplitudes to proceed in our analysis.

III. Results

Figure 2.5 presents the fit to the signal, which consists of 10,000 events. The fit is reasonably good, although it does not perfectly align with the theoretical expectation. This discrepancy can be attributed to issues with event generators such as MadGraph5, which, in this case, produced massless neutrinos in some events, leading to a slight skew in the fit.

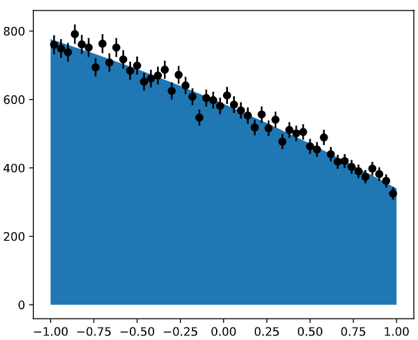

Figure 2.5: Fit to PDF of signal events only.

Figure 2.6 illustrates the fit after applying filtering cuts to both signal and background events. These cuts are effective in significantly reducing the background, but they also reduce the total number of events from 30,000 to approximately 15. As a result, the fit is not perfect, reflecting the challenge of dealing with a higher proportion of background compared to signal in the detector. The distribution of these background and signal events is depicted in Figure 2.7.

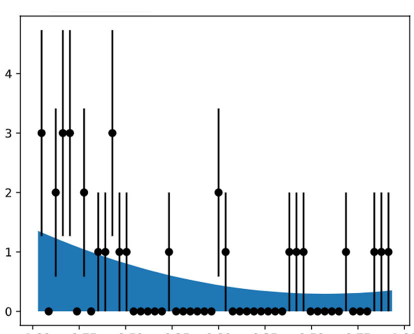

Figure 2.6: Fit to PDF with signal and background events, after applying filtering cuts.

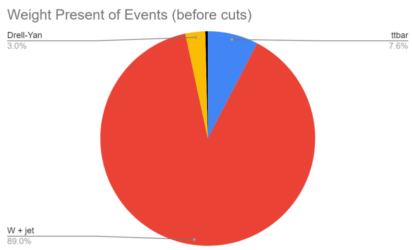

Figure 2.7: Distribution of Signal and Background. Thin black sliver shows the signal events.

IV. Conclusions

This summer's research demonstrates that background processes have a significant impact on the analysis. However, the applied filtering cuts have proven effective in mitigating these effects. Future research will involve applying this methodology to larger datasets, which should yield more accurate and consistent results, as well as facilitate the extraction of the necessary reduced amplitudes. Additionally, efforts will continue to explore strategies for further minimizing the influence of background processes.

[AS24] J. A. Aguilar-Saavedra, *Full quantum tomography of top quark decays*, `https://arxiv.org/abs/2402.14725`, 2024.

2.3 Measuring Entanglement of Orbital and Spin Angular Momenta in Top Quark Decays

G. Miller, *Cleveland State University, Cleveland, OH*; A.T. Arce, *Duke University, Durham, NC*

CERN's Large Hadron Collider (LHC) produces elementary particles using proton collisions. These interactions permit characterization of quantum entanglement, such as how the entanglement of an unstable state is transferred to its decay projects. In this project, the entanglement of the total angular momentum of the top quark with the spins of its decay products (W boson and b quark) is explored. The goal of this work is to build a framework for determining entanglement in top quark decays using simulated LHC data and to provide a first step towards a complete description of the quantum state of top quark decays in LHC collisions. This project recreates the theoretical results from a paper [AS24] using simulated data and further explores how the results are altered when using only observable data.

I. Introduction

At CERN's Large Hadron Collider (LHC), protons accelerate in two opposite beam directions until they are collided. The proton-proton collisions can produce a variety of events, including single top quark decays (see Fig. 2.8). In a single top quark event, the top quark decays into a bottom quark and a W boson, with the W boson becoming a muon and neutrino. The various quarks that are produced are unstable in their current state, so they will continue on to hadronize, which is not shown in the figure.

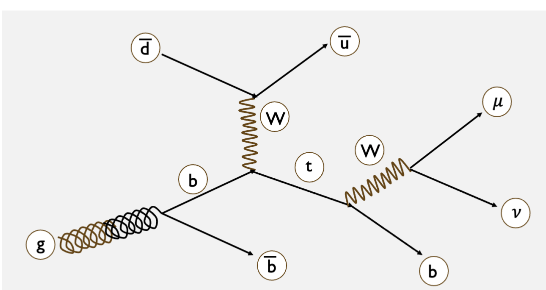

Figure 2.8: The Feynman diagram for single top quark events at the LHC.

At the LHC, there are several detectors used to determine the behavior and activity of the particles after each collision. This project will work specifically with data from the ATLAS detector (see Fig. 2.9). The ATLAS detector provides measurements for several types of particles, however, it is unable to determine the precise four vectors of everything involved in most collisions.

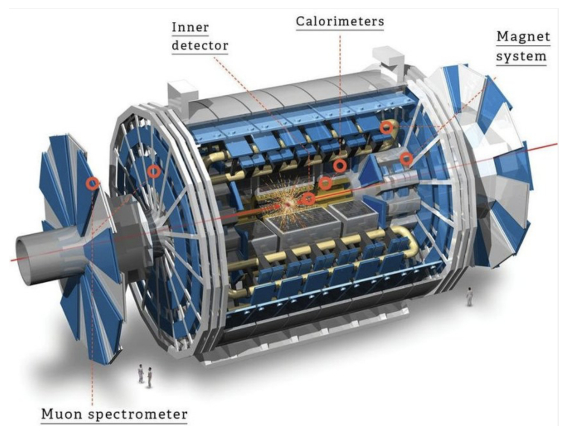

Figure 2.9: Simple schematic of the ATLAS detector [SF17].

Using data from CERN's ATLAS detector, several properties of top quark decays can be explored, including the entanglement of angular and spin momenta. Quantum entanglement is a phenomenon in which the quantum states of two existing particles cannot be described independently of each other, including those at large distances. In quantum mechanics, the entanglement of two quantities is determined using the Peres-Herodecki criterion, which is concerned with the density operator of the system. In the case of single top quark events, the elements of the density operator cannot be directly or easily determined using LHC observables. However, setting up specific reference frames allows for these values to be calculated from measurable data. To build the required reference frames the four vectors of the anti-up quark (spectator jet), muon, neutrino, top quark, bottom quark, and W boson are needed. From these frames, the quantities ϕ, θ, ϕ^*, and θ^* will allow for the W particle's helicity fractions to be calculated [AS24]. These values are well known, and hence can be used to check results as well as provide information about the full quantum state of the top quark.

II. Methods

As previously mentioned, specific reference frames are required to build the complete quantum state of the top quark. These include frames in both the top quark center of mass, as well as the W boson center of mass. The frame in the top center of mass must have the spectator jet's momentum aligned with the z-axis, while assuring the beamline is in the xz-plane. In the top frame, the W boson's momentum angles, θ and ϕ, will contribute to the further analysis required. The second reference frame, or the W frame, requires the W momenta to be aligned with the z' axis, and for y' to remain in the xy-plane and be at an angle of ϕ with y. This frame provides the information for ϕ^* and θ^*, which are the angles of the lepton's momentum vector. Plotting $\cos(\theta^*)$ and fitting it to Eqn. 2.3 allows for the W helicity fractions to be determined [AS24].

$$\frac{1}{\Gamma}\frac{d\Gamma}{d\cos\theta^*} = \frac{3}{8}F_+(1+\cos\theta^*)^2 + \frac{3}{4}F_0\sin^2\theta^* + \frac{3}{8}F_-(1-\cos\theta^*)^2 \tag{2.3}$$

Before incorporating real LHC data, simulations are needed to compare the results with theoretical predictions. With the purpose of recreating theoretical results and building an accurate framework for analysis, a complete knowledge of each particle's four-vectors was initially assumed. The simulations were created with Monte Carlo event generators and Madgraph5, which use underlying theory and high-energy interactions to generate events. Due to the probabilistic nature of particles, a large data set is needed for statistical accuracy; a data set of 10,000 events was used. Several python libraries were used to increase the efficiency of the analysis, including *Vector* for boosts, rotations, and trigonometric values, and *Hist* for plotting.

After completing the analysis with a full set of four-vectors, the results were retested using only LHC observables. This consisted of the four vectors for the up quark, bottom quark, and lepton, as well as an incomplete neutrino vector. Using this limited information, the event was reconstructed and tested to determine the expected deviation that occurs when using only measurable data. The first step of reconstruction was to produce the z-component of the neutrino momentum using the W boson's invariant mass. The x and y components of the neutrino vector are known from the missing transverse energy. Solving for the missing p_z using the invariant W mass results in a quadratic solution, to determine the correct solution, the top quark mass was used to choose the physically realistic momentum. From here, the other four vectors can be easily be determined by adding the vectors of their decay products.

III. Results

Using the methods described above, the distributions for ϕ^* and θ^* can be obtained. From the θ^* values, a histogram of $cos(\theta^*)$ can be fit for the fully simulated data. The histogram and fit are shown in Fig. 2.10. The fit parameters, or the W helicity fractions, for each case are recorded in Fig. 2.13. The results of the helicity fractions from the fully simulated data matched closely to the expected values, an indicator that the analysis was done correctly.

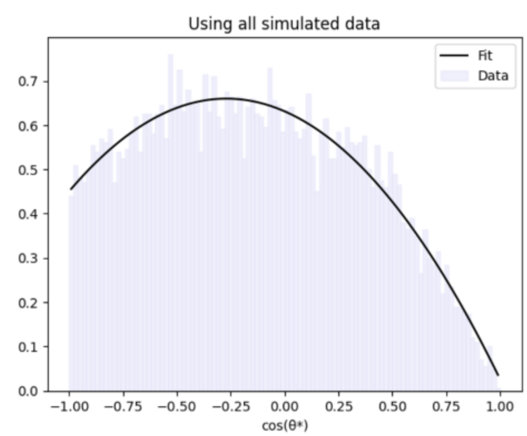

Figure 2.10: Histogram and fit of $\cos(\theta^*)$ for the fully simulated data.

After building the framework for analysis using fully simulated data, it was repeated using only observable quantities. The incomplete four vectors were reconstructed using the methods outlined. This similarly yielded very close results to the expected values (see Fig. 2.11).

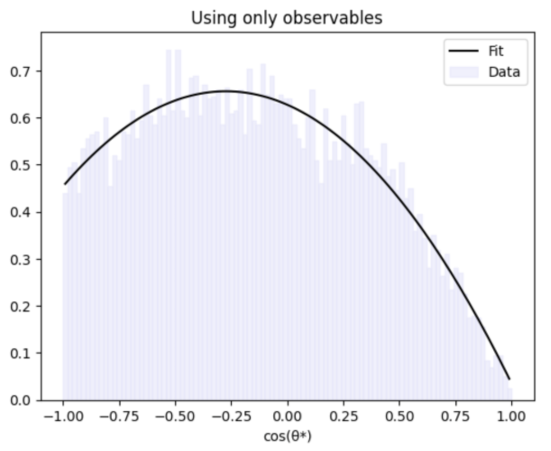

Figure 2.11: Histogram and fit of $\cos(\theta^*)$ using only observable values and reconstructed data.

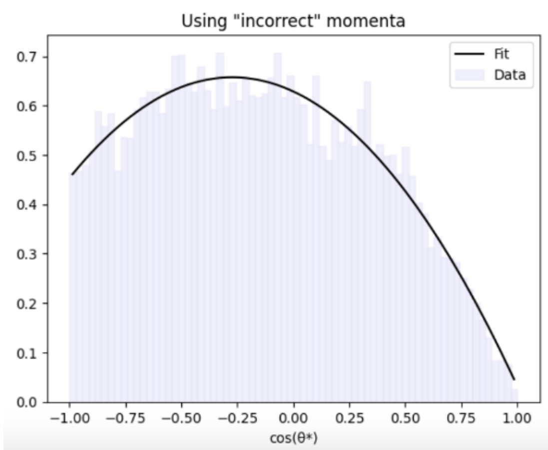

Figure 2.12: Histogram and fit of $\cos(\theta^*)$ for the "incorrect" neutrino p_z events.

To further explore how the error from using only observable quantities affected the results, the "incorrect" neutrino p_z were filtered out from the rest of the events. The term "incorrect" is being used loosely to represent the events in which the chosen p_z was in the opposite direction as the accepted p_z from the simulated data. This error arises primarily due to the W boson and top quark mass not being entirely invariant, as they were assumed to be in the analysis. This portion of events was extremely small, being only a total of .0355% of events. Furthermore, the helicity fractions remained close to the accepted values, showing that event reconstruction has minimal impact on accuracy (see Fig. 2.12)

	Expected	Fully Simulated	Only Observables	"Incorrect" Momenta
F+	0.01	0.018	0.024	0.021
F0	0.69	0.682	0.674	0.676
F-	0.30	0.301	0.303	0.302

Figure 2.13: Table of the determined helicity fractions for each case.

IV. Conclusions

This project sets up a framework for building the full quantum state of top quarks, as well as a basis for using LHC data. This will allow for the exploration of the quantum entanglement of orbital and spin angular momenta in top decays. It was shown that event reconstruction had minimal impact on the W helicity amplitudes. In future work, smearing effects from measurement uncertainty will be incorporated to test how it alters these results.

[AS24] J. A. Aguilar-Saavedra, *Full quantum tomography of top quark decays*, `https://arxiv.org/abs/2402.14725`, 2024.

[SF17] E. Simas Filho *et al.*, In *Proc. XXXV Simpósio Brasileiro de Telecomunicações e Processamento de Sinais (SBrT2017)*, 2017, `10.14209/sbrt.2017.103`.

2.4 Searching for Dark Matter at the LHC Using a Graph Computing Algorithm

K. Bennett, *Haverford College, Haverford, PA*; A.V. Kotwal, *Duke University, Durham, NC*

Dark matter is a hypothetical form of matter thought to make up 25% of the known universe. First proposed in 1933 by astrophysicists, it was postulated as an explanation to gravitational anomalies in the known universe. Unlike baryonic matter, it does not interact with light, electromagnetic radiation, or any known form of matter. Recent theories suggest there exists metastable charged particles that decay invisibly into dark matter [Kot21]. The detection of these particles and proof of the existence of dark matter would mean significant strides in our understanding of gravity and the universe as a whole. This project utilizes a graph computing algorithm implemented on field programmable gate arrays (FPGA) to detect the trajectory of these particles. We use C++ to write programs describing the algorithm as a circuit and simulate the FPGA implementation in software.

I. Introduction

Through the discovery of the Higgs boson at the Large Hadron Collider (LHC) in 2012, physicists have been able to confirm one of the most important building blocks of relativistic quantum field theory of particles and their interactions — the standard model (SM). The SM is the current leading theory that explains three of the four fundamental forces: the weak force, the strong force, and the electromagnetic force. Despite the success of the SM in its predictions, it still is incomplete as it does not yet account for dark matter. Dark matter is a hypothetical form of matter first proposed in 1933 as a possible explanation for gravitational anomalies found in astrophysics. Its interactions on cosmological scales are important for large-scale structure formation. It is thought to make up about 25% of the universe's matter. Unlike baryonic matter, it does not interact with light or any known form of matter which is what has made detecting it through the use of traditional calorimeters and muon sensors very challenging. This project aims to utilize a graph computing algorithm that can be implemented on a field programmable gate array (FPGA) to detect the trajectory (”track”) of charged particle progenitors that may decay invisibly into dark matter within the LHC.

II. Methods

Our method utilizes a graph computing algorithm to cluster spacepoints, created by charged particles, that are recorded by two-dimensional silicon pixel sensors into mathematically-defined patterns that can be used to track the trajectory of these particles [Kot24]. Djisktas algorithm is used alongside Laplacian calculations on groups of three nodes to find a minimum path of trajectory . The spacepoints $h_{i,l}$ created by charged particles are represented in an $i \times l$ matrix where l denotes the point's sensor layer and i denotes the point's ordinal number in that layer. Each spacepoint is associated with an azimuthal ϕ and a longitudinal coordinate z.

The nodes are connected to form a graph that spans the layers and each connection between nodes is given a link weight that is proportional to the the distance between nodes. At each node, a graph operator $\Delta_{ijk,l}$ is defined using triplets of hits $h_{i,l}$,$h_{j,l+1}$, $h_{k,l-1}$ where $h_{j,l+1}$ *and* $h_{k,l-1}$ denotes all possible hits in the previous and forward layer. This operator is used to compute discretized second derivatives (”laplacians”) which are used to construct the minimal trajectory of particles through the graph. By focusing on the initial short travel distances (e.g., 25 cm), this method can detect particles that decay before reaching traditional detection layers. To apply our algorithm to FPGA technology we utilize the Xilinx Vitis HLS and Vivado software programs which allow us to design a circuit based on our algorithm using C++ and visualize the circuit on an FPGA before implementing it at the LHC.

III. Results

Due to challenges in synthesizing the full system circuit, we instead focused on synthesizing smaller parts of the circuit, mainly the patchmaker. The patchmaker is responsible for breaking down spacepoint data from the detector fast enough to be fed into the nodes of the parallel computer running the track-finder circuit. Figure 2.14 shows the implementation of the patchmaker on an xcvu19p-fsvb3824-2-e FPGA device. The diagram shows the grid layout of the FPGA device with each cell corresponding to a configurable logic block (CLB), digital signal processor (DSP), block RAM (BRAM), or other specialized blocks available on the FPGA. The dense cyan cluster in the middle of the grid indicates a high concentration of active elements and connections. This cluster shows what parts of the FPGA are being utilized by our circuit. The high density of the cluster suggests a scenario of high congestion and clustering of circuit elements which could lead to inefficiency and routing delays. It also indicates more power consumption.

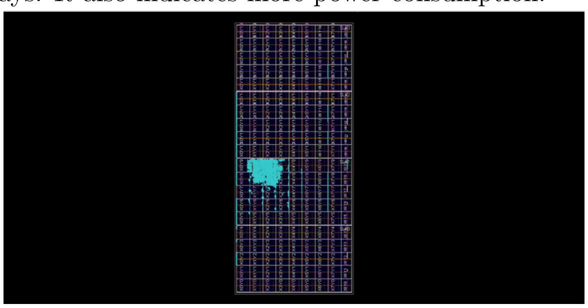

Figure 2.14: Image showing implemented design for the Patchmaker RTL on FPGA Device xcvu19p-fsvb3824-2-e with a 10 ns timing constraint and no I/O delays added to the timing constraints

Figure 2.15 shows the timing summary of the design. This summary shows the slack analysis for setup timing, hold timing, and pulse width timing. Slack refers to the difference between the required arrival time and the actual arrival time of a signal at a timing endpoint. The worst negative slack (WNS) is the highest negative slack value in the circuit and therefore indicates the maximum extent to which the circuit's timing constraints are violated. Looking at Figure 2.15 we can see that the design met the user-specified timing constraints with zero failing endpoints.

Although this result indicates that the design shown in Figure 2.14 is time-efficient within its path, our Vivado suite still indicated critical warnings with regard to Input/Output (I/O) delays on some gates within the design which might have been the source of the clustering and power inefficiency seen in Figure 2.14. Given this, we added a minimum and maximum input delay of 2 and 3 ns respectively as well as a minimum and maximum output delay of 3 and 7 ns to the gates flagged by Vivado as an attempt to fix the issues. The result of this adjustment is shown in Figure 2.16.

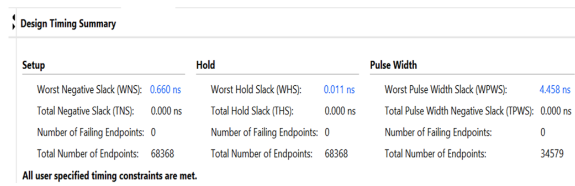

Design Timing Summary

Setup		Hold		Pulse Width	
Worst Negative Slack (WNS):	0.660 ns	Worst Hold Slack (WHS):	0.011 ns	Worst Pulse Width Slack (WPWS):	4.458 ns
Total Negative Slack (TNS):	0.000 ns	Total Hold Slack (THS):	0.000 ns	Total Pulse Width Negative Slack (TPWS):	0.000 ns
Number of Failing Endpoints:	0	Number of Failing Endpoints:	0	Number of Failing Endpoints:	0
Total Number of Endpoints:	68368	Total Number of Endpoints:	68368	Total Number of Endpoints:	34579

All user specified timing constraints are met.

Figure 2.15: Figure showing the design timing summary for the circuit diagram shown in Figure 1. Design timing summary gives all the details relating to the slack of the circuit, specifically, the setup slack, hold slack, and pulse width slack

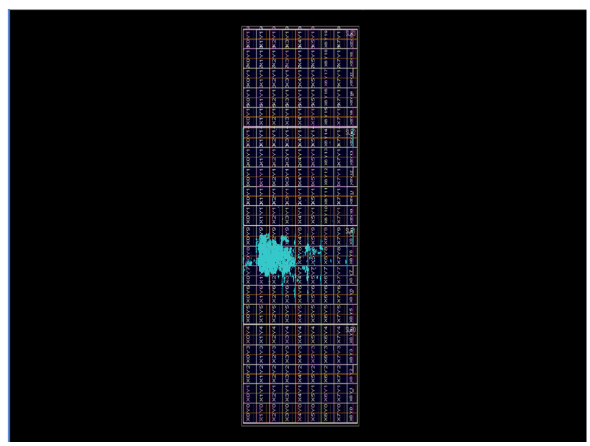

Figure 2.16: Image showing Implemented design for the Patchmaker RTL on FPGA Device xcvu19p-fsvb3824-2-e with a 13.4 ns clock period. The design was implemented with a minimum and maximum input delay of 2 and 3 ns respectively as well as a minimum and maximum output delay of 3 and 7 ns added to the timing constraints

In Figure 2.16 we see that although there is still clustering toward the center of the FPGA the circuit elements are now more horizontally spread compared to the previous design in Figure 2.14. This helps to reduce congestion in vertical interconnects and manages communication between components as well as reduces power consumption. Figure 2.17 details the design timing summary for Figure 2.16 which shows that there is significantly worse setup slack in this implementation than the previous one. This suggests that the I/O constraints added to the circuit may not have been properly timed and implemented. A deeper investigation into the circuit components and paths using Vivado showed variation in the slack of different paths each requiring specified constraints.

Figure 2.17: Figure showing the design timing summary for the circuit diagram shown in figure 3. Design timing summary gives all the details relating to the slack of the circuit, specifically, the setup slack, hold slack, and pulse width slack

Additionally, the issue could lie within the routing and placement of the circuit components. In this case, we can experiment with different combinations of the Vivado synthesis and implementation tools outside of just the default settings.

IV. Conclusions

Our results have revealed that our current source code is quite inefficient and needs to be optimized to reduce the complexity of the circuit for easier implementation. Despite the circuit not functioning as initially planned, our results show that our preliminary designs of the patchmaker are heading in the right direction. Our visualization of the circuit design and schematic gives us insight into the full system despite the fact we are still unable to produce the full system circuit due to random access memory (RAM) issues. In continuing this project, we hope to develop a new version of the current patchmaker that is both time- and power-efficient. Furthermore, we hope to implement and visualize the full system in Vivado.

[Kot21] A. V. Kotwal, Sci. Rep., **11**, 18543 (2021).

[Kot24] A. V. Kotwal *et al.*, Sci. Rep., **14**, 10181 (2024).


MAC
EVENT STAFF


CAROLINA